Intrinsic Morphology of Ultra-diffuse Galaxies

Rong, Yu; Dong, Xiao-Yu; Puzia, Thomas H.; Galaz, Gaspar; Sanchez-Janssen, Ruben; Cao, Tianwen; van der Burg, Remco F. J.; Sifon, Cristobal; Pina, Pavel E. Mancera; Marcelo, Mora

Published in:
Astrophysical Journal

DOI:
10.3847/1538-4357/aba74a

Publication date:
2020

The Astrophysical Journal, 899:78 (15pp), 2020 August 10 https://doi.org/10.3847/1538-4357/aba74a

Intrinsic Morphology of Ultra-diffuse Galaxies

Yu Rong[1,16], Xiao-Yu Dong[2], Thomas H. Puzia[1], Gaspar Galaz[1], Ruben Sánchez-Janssen[3], Tianwen Cao[1,4,5,6], Remco F. J. van der Burg[7], Cristóbal Sifón[8,9], Pavel E. Mancera Piña[10,11], Mora Marcelo[1], Giuseppe D'Ago[1], Hong-Xin Zhang[12,13], Evelyn J. Johnston[1,16], and Paul Eigenthaler[1,14,15]

[1] Institute of Astrophysics, Pontificia Universidad Católica de Chile, Av. Vicuña Mackenna 4860, 7820436 Macul, Santiago, Chile; rongyuastrophysics@gmail.com
[2] Department of Physics and Astronomy, California State University, Northridge, CA 91330, USA
[3] STFC UK Astronomy Technology Centre, Royal Observatory, Blackford Hill, Edinburgh, EH9 3HJ, UK
[4] Chinese Academy of Sciences South America Center for Astronomy, National Astronomical Observatories, Chinese Academy of Sciences, Beijing 100012, People's Republic of China
[5] Key Laboratory of Optical Astronomy, National Astronomical Observatories, Chinese Academy of Sciences, Beijing 100101, People's Republic of China
[6] School of Astronomy and Space Science, University of Chinese Academy of Sciences, Beijing 100049, People's Republic of China
[7] European Southern Observatory, Karl-Schwarzschild-Str. 2, D-85748, Garching, Germany
[8] Instituto de Física, Pontificia Universidad Católica de Valparaíso, Casilla 4059, Valparaíso, Chile
[9] Department of Astrophysical Sciences, Peyton Hall, Princeton University, Princeton, NJ 08544, USA
[10] Kapteyn Astronomical Institute, University of Groningen, Lanleven 12, 9747 AD, Groningen, The Netherlands
[11] ASTRON, the Netherlands Institute for Radio Astronomy, Postbus 2, 7990 AA, Dwingeloo, The Netherlands
[12] CAS Key Laboratory for Research in Galaxies and Cosmology, Department of Astronomy, University of Science and Technology of China, People's Republic of China
[13] School of Astronomy and Space Sciences, University of Science and Technology of China, Hefei 230026, People's Republic of China
[14] Astro-Engineering Center of the Catholic University (AIUC), Av. Vicuña Mackenna 4860, 7,820,436 Macul, Santiago, Chile
[15] Max-Planck-Institut für Astronomie, Königstuhl 17, D-69117 Heidelberg, Germany
Received 2019 July 22; revised 2020 June 13; accepted 2020 July 18; published 2020 August 14

Abstract

With the published data of apparent axis ratios for 1109 ultra-diffuse galaxies (UDGs) located in 17 low-redshift ($z \sim 0.020$–0.063) galaxy clusters and 84 UDGs in two intermediate-redshift ($z \sim 0.308$–0.348) clusters, we take advantage of a Markov Chain Monte Carlo approach and assume a triaxial model to investigate the intrinsic morphologies of UDGs. In contrast to the conclusion of Burkert, i.e., the underlying shapes of UDGs are purely prolate ($C = B < A$), we find that the data favor the oblate-triaxial models (i.e., thick disks with $C < B \lesssim A$) over the nearly prolate ones. We also find that the intrinsic morphologies of UDGs are related to their stellar masses/luminosities, environments, and redshifts. First, the more luminous UDGs have puffier morphologies compared with the less luminous counterparts; the UDG morphologic dependence on luminosity is distinct from that of the typical quiescent dwarf ellipticals (dEs) and dwarf spheroidals (dSphs); in this sense, UDGs may not be simply treated as an extension of the dE/dSph class with similar evolutionary histories; they may differ not only in size. Second, the UDGs with smaller clustercentric distances are more puffed up, compared with the counterparts with larger clustercentric distances; in combination with the UDG thickness dependence on luminosity, the puffier morphologies of UDGs with high luminosities or located in the denser environments are very likely to be attributed to tidal interactions with massive galaxies. Third, we find that the intermediate-redshift UDGs are more flattened, compared with the low-redshift counterparts, which plausibly suggests a "disky" origin for the high-redshift, newly born UDGs.

Unified Astronomy Thesaurus concepts: Dwarf galaxies (416); Galaxy evolution (594); Galaxy photometry (611)

1. Introduction

The investigations of the properties and formation of ultra-diffuse galaxies (UDGs; van Dokkum et al. 2015) with Milky Way sizes but luminosities of typical dwarfs, which were first reported about three decades ago (Sandage & Binggeli 1984; Caldwell & Bothun 1987; Impey et al. 1988; Conselice et al. 2003), have not reached a clear consensus. The high-redshift strong feedback model agrees that UDGs may be failed L^* galaxies embedded in massive halos but that ceased their in situ star formation in the early universe (e.g., Yozin & Bekki 2015); the observations for the largest UDG in the Coma cluster, DF 44, also support UDGs to be hosted in massive halos with total masses of $M_{\rm h} \sim 10^{12}\,M_{\odot}$ (van Dokkum et al. 2016). However, the semi-analytic galaxy formation models and some hydrodynamical simulations prefer UDGs to populate the relatively lower mass halos $M_{\rm h} \sim 10^{9}$–$10^{11}\,M_{\odot}$, which originated from the high specific angular momentum of their host halos or outflows (e.g., Amorisco & Loeb 2016; Di Cintio et al. 2017; Rong et al. 2017a); the halo masses for the UDGs located in galaxy clusters, estimated from the empirical relation between masses of member globular cluster system and their parent halo (e.g., Beasley et al. 2016; Beasley & Trujillo 2016; Peng & Lim 2016; Prole et al. 2019), as well as the gravitational lensing technique (Sifón et al. 2018), support that UDGs may be genuine dwarfs; the morphological and structural classifications and stellar population properties of many UDGs were found to be similar to those of the dE/dSphs, also suggesting that UDGs and dE/dSphs are taken from the same population and differ only in size (Wittmann et al. 2017; Conselice 2018); the H I detections for the UDGs located in the low-density environments reveal the relatively higher specific angular momenta of these field UDGs, compared with those of the typical dwarf counterparts (Leisman et al. 2017). Other possible origins, including tidal interaction, supernova energy

[16] FONDECYT Postdoctoral Fellow.

injection, etc. (Conselice 2018; Jiang et al. 2019; Ogiya 2018; Carleton et al. 2019; Liao et al. 2019; Martin et al. 2019), are also plausibly supported by the controversial photometric tidal/interaction evidence (e.g., Bennet et al. 2018; Greco et al. 2018; Müller et al. 2019), as well as spectroscopic results (Struble 2018; Chilingarian et al. 2019; Martín-Navarro et al. 2019); particularly, the recent findings of lack of dark matter in two member UDGs in the NGC 1052 group, NGC 1052-DF2 and NGC 1052-DF4, possibly suggest an outstanding role of tidal stripping in UDG evolution (Ogiya 2018; van Dokkum et al. 2018, 2019; Danieli et al. 2019).

For the member UDGs in the low-density and high-density environments, they primarily populate the blue cloud and red sequence (RS) in the color–magnitude diagram, respectively (e.g., Mihos et al. 2015; van der Burg et al. 2016; Janssens et al. 2017; Lee et al. 2017; Román & Trujillo 2017a, 2017b; Venhola et al. 2017; Spekkens & Karunakaran 2018; Rong et al. 2020b); their morphologies are also distinct: the former ones are mostly irregular, while the latter ones usually have elliptical appearances (e.g., Yagi et al. 2016; Leisman et al. 2017; Román & Trujillo 2017a; Trujillo et al. 2017; Conselice 2018; Eigenthaler et al. 2018). A large fraction of UDGs in galaxy clusters exhibit unresolved nuclear star clusters (e.g., Mihos et al. 2015; Yagi et al. 2016; Eigenthaler et al. 2018). Several UDGs show clear evidence for association with tidal material and interaction with a larger galaxy halo (e.g., Toloba et al. 2016; Bennet et al. 2018). These photometric evidences suggest the diverse morphologies of UDG populations and plausibly imply the evolution of UDG intrinsic morphologies with redshifts and environments, which further provide a clue to the formation and evolution of UDGs.

According to the distribution of the apparent axis ratios $q = b/a$ of the Coma UDGs, in particular, the absence of UDGs with $q > 0.9$, Burkert (2017) claimed that the on-average intrinsic shapes of the cluster UDGs are more likely to be purely prolate (i.e., the three intrinsic axes of UDGs satisfy $C = B < A$), compared with a purely oblate disk model (i.e., $C < B = A$); the strong radial alignment signals[17] of cluster UDGs (e.g., Yagi et al. 2016; van der Burg et al. 2017) may also prefer a prolate model. However, it is worth noting that a more reasonable diagnostic for the underlying morphologies of UDGs is to assume a prevalent triaxial ($C \leqslant B \leqslant A$) model, rather than to simply choose between the purely prolate and purely oblate models. Specifically, the sharply reduced number of Coma UDGs with $q > 0.9$ in the q distribution can also be well explained by an oblate-triaxial model (e.g., Binney & Merrifield 1998, see Section 4.3.3 and Figure 4.36), except for the purely prolate model.

Therefore, the three-dimensional (3D) morphologies of UDGs should be carefully studied again with a triaxial model. We aim to analyze the possible evolution of UDG morphologies from, e.g., low-density to high-density environments, high redshifts to low redshifts, low mass to high mass, etc. In Section 2, we introduce the UDG samples studied in this work and show the distributions of their apparent axis ratios. In Section 3, we investigate the intrinsic shapes of UDGs by assuming a triaxial model and study the possible morphology evolution of UDGs. We summarize our results in Section 4.

[17] There is also literature that alternatively suggests no UDG radial alignment in some galaxy clusters (Mancera Piña et al. 2019; Rong et al. 2019), but possible UDG primordial alignment (Rong et al. 2020a).

Table 1
Information of the Parent Galaxy Clusters/Groups Where the UDG Samples Are Located

Clusters	z	R_{200} (Mpc)	$N_{\rm inner}$	$N_{\rm middle}$	$N_{\rm outer}$
Coma[a]	0.023	2.6[b]	204	124	0
R1204[c]	0.020	0.6	7	15	17
A779[c]	0.023	0.7	7	17	7
R1223[c]	0.026	0.6	10	7	20
MKW4S[c]	0.027	0.6	5	9	28
R1714[c]	0.028	0.4	2	6	35
A2634[c]	0.031	1.3	51	61	8
A1177[c]	0.032	0.7	5	9	25
A1314[c]	0.033	0.9	16	20	55
A119[d]	0.044	1.9	38	18	0
MKW3S[d]	0.044	1.2	8	10	0
A85[d]	0.055	2.0	37	30	0
A780[d]	0.055	1.7	11	23	0
A133[d]	0.056	1.7	27	27	0
A1991[d]	0.059	1.2	17	8	0
A1781[d]	0.062	0.9	4	12	0
A1795[d]	0.063	1.6	22	47	0
A2744[e]	0.308	2.4	26	13	0
AS1063[e]	0.348	2.5	33	6	6

Notes. Column (1): cluster name. Column (2): redshift. Column (3): virial radius R_{200} (Mpc). Columns (4)–(6): numbers of UDGs in $R \leqslant 0.5\,R_{200}$, $0.5\,R_{200} < R \leqslant R_{200}$, and $R > R_{200}$, respectively.
[a] Yagi et al. (2016).
[b] Brilenkov et al. (2015).
[c] Mancera Piña et al. (2019).
[d] van der Burg et al. (2016).
[e] Lee et al. (2017).

2. UDG Data

2.1. UDG Samples

The UDG samples used in this work are gathered from the previous literature, located in 17 low-redshift (low-z; $z \sim 0.020$–0.063) clusters/groups and two intermediate-redshift (intermediate-z; $z \sim 0.308$–0.348) clusters, as listed in Table 1. Almost all of these UDGs follow the RS in the color–magnitude diagram.

Sample 1: the publicly available[18] Coma UDG sample reported by Yagi et al. (2016). These UDGs are distributed within R_{200} (R_{200} is the radius within which the mean cluster density is 200 times the critical density) of Coma, with r-band[19] absolute magnitudes of $-17\ {\rm mag} < M_r < -9\ {\rm mag}$, effective radii $r_{\rm e} > 1.5$ kpc, and mean surface brightness within $r_{\rm e}$, $\langle \mu_{\rm e}(r) \rangle$, between 24 and 27 mag arcsec^{-2}. Only 1% of UDGs show Sérsic indices of $n > 2$.

Sample 2: UDGs selected by Mancera Piña et al. (2019), located in both the inner (within the virial radii) and outer (beyond the virial radii) regions of eight low-z clusters. UDGs were selected with $r_{\rm e} > 1.5$ kpc, $\langle \mu_{\rm e}(r) \rangle > 24$ mag arcsec^{-2},

[18] http://vizier.cfa.harvard.edu/viz-bin/VizieR?-source=J/ApJS/225/11

[19] The original magnitude and surface brightness values of UDGs in Yagi et al. (2016) are in the R band; in order to compare the surface brightness and magnitudes of the Coma UDGs with those of the other UDG samples, we convert the R-band surface brightnesses and magnitudes to r-band properties with $R - r = \sum_{k=0}^{7} c_k (r - i)^k \sim 0.08$ mag (Yagi et al. 2016), where the colors of the cluster UDGs approximately are $r - i \sim 0.25$ (e.g., Rong et al. 2017a), and constants c_k are obtained from Table 2 in Yagi et al. (2016). Indeed, the R- and r-band magnitudes/surface brightness levels only show a marginal difference.

and $n < 4$ (only <3% UDGs have $n > 2$); these UDGs have absolute magnitudes of -18 mag $< M_r < -12.5$ mag.

Sample 3: UDGs in eight low-z clusters selected by van der Burg et al. (2016). Only the UDG candidates with circular effective radii of $r_{e,c} = r_e\sqrt{b/a} \in (1.5, 7.0)$ kpc (b/a denotes the elongation of a galaxy), $\langle\mu_e(r)\rangle \in (24.0, 26.5)$ mag arcsec^{-2}, and $n < 2$ are included. All of these UDGs are distributed within the virial radii of clusters.

Sample 4: the publicly available[20] UDG sample in the two intermediate-z clusters, A2744 and AS1063 (Lee et al. 2017). UDGs were selected with $r_{e,c} > 1.5$ kpc and $\langle\mu_{e,abs}(r)\rangle > 23.8$ mag arcsec^{-2} ($\langle\mu_{e,abs}(r)\rangle = \langle\mu_{e,z}(r)\rangle - 10\log(1+z) - E(z) - K(z)$ (Graham & Driver 2005), where $\langle\mu_{e,abs}(r)\rangle$ and $\langle\mu_{e,z}(r)\rangle$ are the mean surface brightness at $z = 0$ and z, respectively, and the values of $E(z)$ and $K(z)$ are -0.36 and $+0.11$ for AS1063 and -0.32 and $+0.09$ for A2744, respectively (see Lee et al. 2017), which corresponds to the surface brightness criterion of sample 3, i.e., $\langle\mu_{e,z=0.055}(r)\rangle > 24.0$ mag arcsec^{-2}. Here 90% of UDGs show $n < 2$.

The apparent axis ratio $q = b/a$ and its error for the spheroid of each UDG in the four studies were obtained from GALFIT (Peng et al. 2002, 2010) fitting with a Sérsic profile,[21] by the authors of the corresponding studies.

2.2. Apparent Axis Ratios of UDGs

Note that the four UDG samples were detected by the different telescopes, and thus the faint ends (for the four samples, the UDG faint ends of $\langle\mu_{e,abs}(r)\rangle$ are ~27.0, 26.5, 26.5, and 26.6 mag arcsec^{-2}, respectively) and detection completeness of the four UDG samples are slightly different. If we assume that the detection completeness of the faintest UDGs is related to their apparent axis ratios (i.e., the edge-on (face-on) oblate (prolate) galaxies perhaps are easier to detect owing to their brighter surface brightness, compared with the face-on (edge-on) ones with the same intrinsic 3D light distribution), the incompleteness of the faint-end UDGs may therefore introduce a bias in the following studies of intrinsic morphologies. Analogously, the four UDG samples adopt a similar UDG bright-end definition of $\langle\mu_{e,abs}(r)\rangle > 24$ mag arcsec^{-2}, which may also cause an absence of the edge-on (face-on) oblate (prolate) UDGs and lead to a bias in this work. Therefore, for each UDG sample, we change the surface brightness faint end and bright end of selecting UDGs and test whether the distribution of the apparent axis ratios $q = b/a$ changes with the different criteria. As explored in Figure 1, for each UDG sample, the q distributions (the 68% Wilson interval (Wilson 1927; Brown et al. 2001) for the probability of each bin is estimated, as shown by the error bar in the distribution) for the different faint ends and bright ends are consistent with each other within the 1σ uncertainties; the two-sample Kuiper tests between the subsamples (colored) with the different criteria and entire sample (black) also return large p values, as shown in Figure 1, suggesting that the faint and bright ends for the four UDG samples will not affect our following studies of UDG intrinsic morphologies.

In Figure 2, we compare the q distributions of UDGs in the four different samples. We find that the three low-z UDG samples show very similar q distributions, i.e., flat in the range of $q \in [0.4, 0.9]$ but decreasing drastically in the ranges of $q < 0.4$ and $q > 0.95$. Therefore, hereafter the three samples will be combined and treated as one low-z UDG sample in the following studies. We also find that, compared with the q distributions of the low-z samples (the blue, magenta, and green histograms), the intermediate-z UDG sample (the red histogram) exhibits a plausibly less flat distribution, which resembles a "double-peak" distribution peaking at $q \simeq 0.53$ and 0.77, respectively. It may imply a UDG morphology evolution with redshifts.

It has been known that the properties of UDGs are related to environment and stellar mass (Román & Trujillo 2017a; Gu et al. 2018). For the low-z UDGs, in order to investigate whether their morphologies evolve from the outside to the inner regions of galaxy clusters, we split the low-z UDGs into three groups, i.e., the inner sample within $R/R_{200} \leqslant 0.5$ (R denotes the projected distance from a galaxy to the center of its parent cluster), the middle sample within $0.5 < R/R_{200} \leqslant 1.0$, and the outer sample within $R/R_{200} > 1.0$. Since the lack of UDGs in the innermost cluster regions has been reported (e.g., van der Burg et al. 2016; Rong et al. 2017a; Mancera Piña et al. 2018) and we may expect a distinct UDG axis ratio distribution, we also plot the q distribution for the innermost sample within $R < 0.2R_{200}$. As shown in the top panel of Figure 3, from the outer to inner region, the median value of the apparent axis ratios increases with the decreasing R/R_{200}, from $q_{median} = 0.61^{+0.22}_{-0.17}$ for the outer sample, to $0.69^{+0.16}_{-0.21}$ for the middle sample, and finally to $0.70^{+0.17}_{-0.19}$ for the inner sample (for the innermost sample, $q_{median} = 0.70^{+0.19}_{-0.17}$, similar to that of the inner-region sample), suggesting that UDGs become rounder toward the denser environments, which is possibly caused by tidal stripping and heating (Moore et al. 1996; Lisker et al. 2006; Aguerri & González-García 2009; Rodriguez-Gomez et al. 2017; Jiang et al. 2019; Ogiya 2018; Carleton et al. 2019), stellar feedback (Pontzen & Governato 2012; Teyssier et al. 2013; El-Badry et al. 2016), etc. For the intermediate-z UDG sample, because of the small galaxy number, we cannot split them into the different R/R_{200} ranges and study their possible morphology evolution with the weak statistical power.

We also divide the low-z UDG sample into the two subsamples with the relatively high ($M_r < -15.2$ mag) and low ($M_r > -15.2$ mag) luminosities (the low-z UDG luminosities range in $M_r \in (-18, -12)$ mag, and $M_r = -15.2$ mag is the median luminosity; see Figure 11) and compare their q distributions in the bottom panel of Figure 3. UDGs with the lower luminosities seem to be more elliptical compared with the ones with the relatively higher luminosities. Since the low-z cluster UDGs show similar colors (e.g., Rong et al. 2017a), we can roughly assume a uniform stellar mass-to-light ratio[22] for these UDGs; therefore, the results also suggest that the high-mass UDGs are rounder than the low-mass ones.

Note that if the spatial distribution preferences of the high-mass and low-mass UDGs are different, the dependence of q on luminosity/stellar mass may be actually caused by the dependence on environment, or vice versa. Therefore, we compare the distributions of R/R_{200} for the high-mass and low-mass UDG samples, as shown in panel (A) of Figure 4; we also divide both of the high-mass and low-mass UDG samples into

[20] http://vizier.cfa.harvard.edu/viz-bin/VizieR?-source=J/ApJ/844/157

[21] These UDGs have been visually inspected to verify whether GALFIT provides a proper fit to the data; the bad ones were abandoned by those authors.

[22] $M_*/L_r \sim 1.96$ (Carleton et al. 2019); $M_r \in (-18, -12)$ mag, roughly corresponding to $(10^7, 10^9)$ $M_\odot$; $M_r = -15.2$ mag, roughly corresponding to $10^{8.2}$ $M_\odot$.

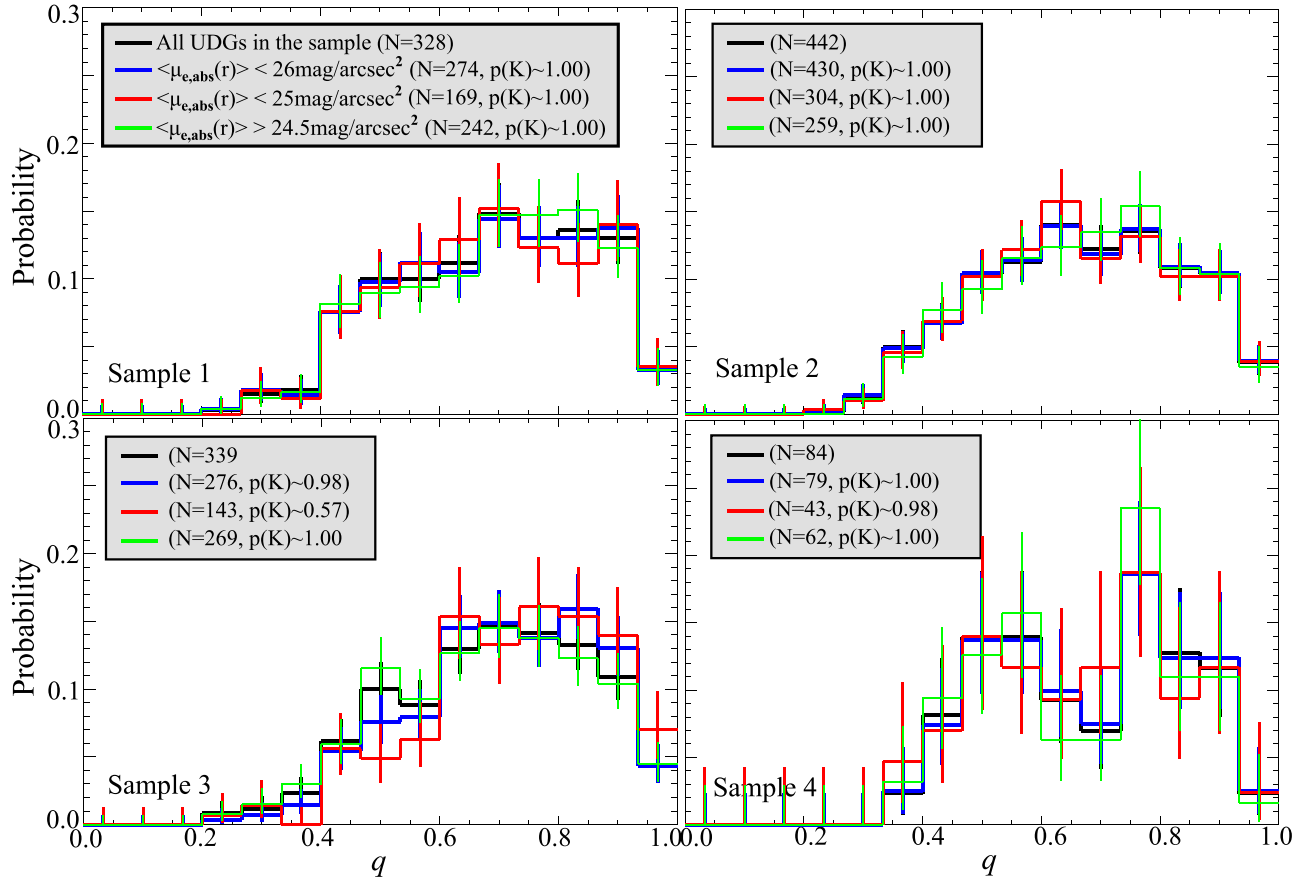

Figure 1. Distributions of q for the four different UDG samples, described in Section 2.1. In each panel, the black, blue, red, and green histograms highlight the distributions of q for the whole sample and UDGs with $\langle\mu_{\rm e,abs}(r)\rangle < 26.0$ mag arcsec^{-2}, $\langle\mu_{\rm e,abs}(r)\rangle < 25.0$ mag arcsec^{-2}, and $\langle\mu_{\rm e,abs}(r)\rangle > 24.5$ mag arcsec^{-2}, respectively. The values N and p(K) in the legends indicate the numbers of UDGs and p values returned from the two-sample Kuiper tests between the entire sample (black) and subsamples (colored) with the different criteria, respectively. Hereafter, the error bars in distributions show the 68% Wilson intervals by assuming the binomial statistics.

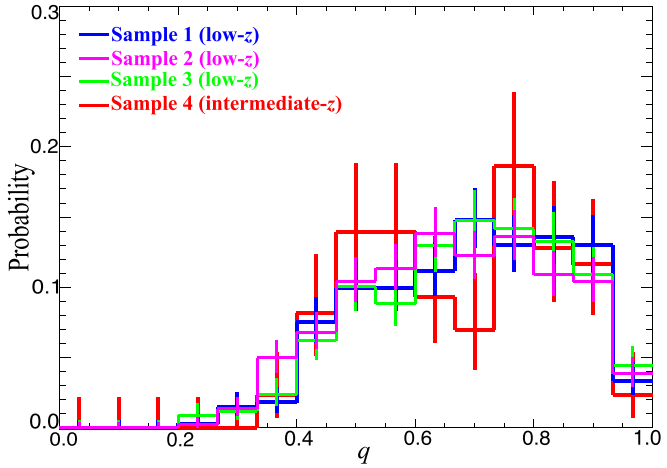

Figure 2. Apparent axis ratio $q = b/a$ distributions of the four UDG samples studied in this work.

the inner ($R < R_{200}$) and outer ($R > R_{200}$) subsamples, and we compare their axis ratios in panels (B) and (C) of Figure 4. Apparently, the spatial distributions of the high-mass and low-mass UDGs are barely different (panel (A)), whereas the q distributions for the four subsamples with the different luminosities and locations are quite different (panel (B)). We find that both the high-mass and low-mass UDG samples located in $R > R_{200}$ are more elliptical compared with their counterparts located in $R < R_{200}$; both of the inner-region and outer-region low-mass UDGs are more elliptical compared with the high-mass counterparts. The results indicate that the morphologies of low-z UDGs depend on both the luminosity and environment.

We also use two-sample Kolmogorov–Smirnov (K-S) tests to evaluate the differences between the q distributions of the UDG subsamples within the different luminosity ranges, R/R_{200} ranges, and redshifts. The p values from the K-S tests are listed in Table 2. Using the Bonferroni correction with an overall significance level of 95% (Miller 1966), we find that, for the low-z UDGs, there may be relatively significant q differences between the low-mass UDG subsamples located in $R \leqslant 0.5\,R_{200}$ and $R > R_{200}$ and between the $R \geqslant 0.5R_{200}$ UDG subsamples with the relatively low and high masses; in addition, the q differences between the high-mass UDG subsamples located in and beyond R_{200} may be moderate (considering the Bonferroni correction with an overall significance level of 68%). Yet, the low-z UDGs in $R < 0.5R_{200}$ and $0.5R_{200} < R < R_{200}$ show weak/no q differences; the differences between the low-z and intermediate-z UDG counterparts are also mild. In general, the K-S test results

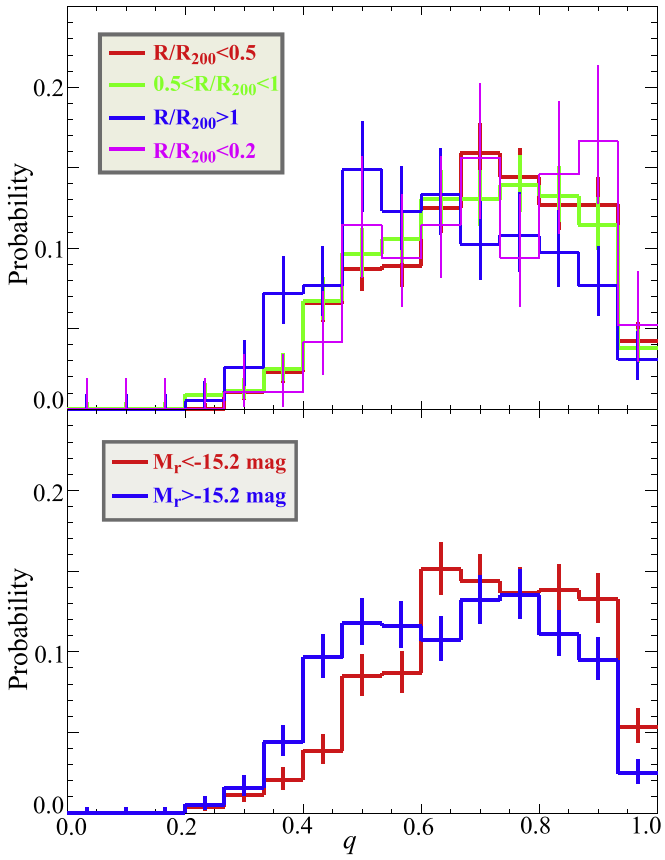

Figure 3. Top: q distributions for the low-z UDGs located in the inner ($R \leqslant 0.5R_{200}$; red), middle ($0.5R_{200} \leqslant R < R_{200}$; green), outer ($R > R_{200}$; blue), and innermost ($R < 0.2R_{200}$) regions, respectively. Bottom: q distributions for the low-z more luminous ($M_r < -15.2$ mag; red) and less luminous ($M_r > -15.2$ mag; blue) UDGs, respectively.

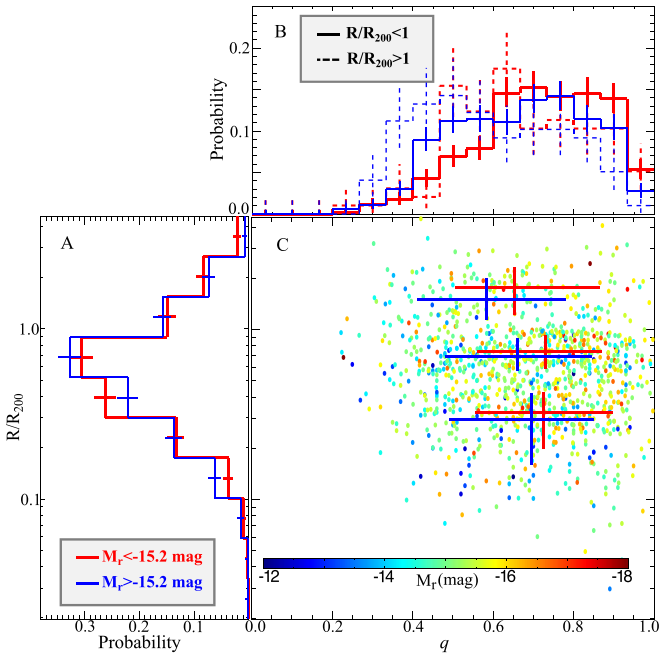

Figure 4. (A) Distributions of R/R_{200} for the low-z high-mass ($M_r < -15.2$ mag; red) and low-mass ($M_r > -15.2$ mag; blue) UDGs. (B) Distributions of q for the low-z high-mass (red) and low-mass (blue) UDGs located in $R < R_{200}$ (solid) and $R > R_{200}$ (dashed), respectively. (C) Colored dots show q vs. R/R_{200} for the entire low-z UDG sample; their colors denote M_r, as shown by the inset color bar; the error bars indicate the median values and 1σ scatters of q and R/R_{200} for the low-z high-mass (red) and low-mass (blue) UDGs located in $R \leqslant 0.5\,R_{200}$, $0.5\,R_{200} < R \leqslant R_{200}$, and $R > R_{200}$.

imply that the morphologies of UDGs may be related to their luminosities and environments (i.e., located in or beyond R_{200}), whereas the morphologic dependence on redshift may be mild/negligible.

3. Intrinsic Morphologies of UDGs

3.1. Modeling

In this section, we will take advantage of a Markov Chain Monte Carlo (MCMC) approach to investigate the intrinsic morphologies of UDGs in the different samples. The method described in Sánchez-Janssen et al. (2016) is used to analyze the intrinsic morphologies of UDGs. Here we briefly outline the key points of the method. In this method, the galaxies in each sample are modeled as a family of optically thin triaxial ellipsoids. The 3D galaxy density is structured as a set of co-aligned ellipsoids characterized by a common ellipticity $E = 1 - C/A$ and a triaxiality $T = (A^2 - B^2)/(A^2 - C^2)$, where $A \geqslant B \geqslant C$ are the intrinsic major, intermediate, and minor axes of the ellipsoid, respectively (Franx et al. 1991). The purely prolate (oblate) model corresponds to $T \simeq 1$ ($T \simeq 0$).

For each UDG sample, their E and T are proposed to follow Gaussian distributions, with mean values and standard deviations of $\bar{E}$, σ_E, $\bar{T}$, and σ_T. Given the distribution of intrinsic axis ratios and random viewing angles for the model galaxies, the distribution of apparent axis ratios q can be derived via projecting these ellipsoids (Rong et al. 2015a; see the Appendix for the projecting method details). Therefore, conversely, the posterior probability density function (pdf) of the model parameters $\bar{E}$, σ_E, $\bar{T}$, and σ_T, representing the intrinsic shapes of each UDG population, can also be inferred by applying a Bayesian framework (see Sánchez-Janssen et al. 2016) and assuming the prior probabilities of $\bar{E}$ and $\bar{T}$ to follow uniform distributions in [0, 1], as well as σ_E and σ_T to follow $p(\sigma) \propto \sigma^{-1}$. We implement the EMCEE code (Foreman-Mackey et al. 2013) to sample the posterior distribution of the model parameters with 200 "walkers" and 1500 steps (the steps are sufficient for the MCMC chains to reach equilibrium).

The modeling results for the different UDG samples are summarized in Table 3. In Figures 5–8, we plot the posterior distributions of $\bar{E}$, σ_E, $\bar{T}$, and σ_T for the low-z and intermediate-z UDG samples, respectively. The posterior distributions for $\bar{E}$ and σ_E approximately resemble the single Gaussian distributions. However, for the low-z UDG samples, the posterior distributions of $\bar{T}$ always show double peaks (see also Appendix A), i.e., one pronounced peak at $\bar{T} \sim 0.3 - 0.4$ and one weak peak at $\bar{T} \sim 1.0$; for the intermediate-z sample, the posterior distribution of $\bar{T}$ exhibits no significant $\bar{T} \sim 1.0$ peak. The two $\bar{T}$ peaks indicate two different probable underlying shapes for the low-z UDGs: the left $\bar{T} \sim 0.3$–0.4 peak corresponds to a triaxial model, and the right $\bar{T} \sim 1.0$ peak corresponds to a purely prolate model. We note that, although the precise triaxiality distribution can only be well derived with a synergy of structural and kinematical data (e.g., Franx et al. 1991; van den Bosch & van de Ven 2009; Rong et al. 2018a; Chilingarian et al. 2019), rather than with the photometric data alone, the data clearly favor triaxial models

Table 2
p Values from Two-sample K-S Tests for the Different UDG Samples

Compared Subsample Pairs in K-S Tests			K-S p Value
Low-z	$M_r < -15.2$ mag	$R \leqslant 0.5\,R_{200}$ versus $0.5\,R_{200} < R \leqslant R_{200}$	8.2×10^{-1}
		$R \leqslant 0.5\,R_{200}$ versus $R > R_{200}$	1.2×10^{-2}
		$0.5\,R_{200} < R \leqslant R_{200}$ versus $R > R_{200}$	3.6×10^{-2}
	$M_r > -15.2$ mag	$R \leqslant 0.5\,R_{200}$ versus $0.5\,R_{200} < R \leqslant R_{200}$	3.7×10^{-1}
		$R \leqslant 0.5\,R_{200}$ versus $R > R_{200}$	1.6×10^{-4}
		$0.5\,R_{200} < R \leqslant R_{200}$ versus $R > R_{200}$	7.2×10^{-3}
	$R \leqslant 0.5\,R_{200}$	$M_r < -15.2$ mag versus $M_r > -15.2$ mag	6.8×10^{-2}
	$0.5\,R_{200} < R \leqslant R_{200}$	$M_r < -15.2$ mag versus $M_r > -15.2$ mag	6.9×10^{-4}
	$R > R_{200}$	$M_r < -15.2$ mag versus $M_r > -15.2$ mag	1.7×10^{-3}
$R \leqslant R_{200}$	$M_r < -15.2$ mag	low-z versus intermediate-z	2.6×10^{-1}
	$M_r > -15.2$ mag	low-z versus intermediate-z	1.8×10^{-1}

Note. In each line, we compare the axis ratios of the two UDG subsamples selected with the criteria listed in the first three columns. The first two columns show the common properties of the two compared subsamples, while the third column exhibits the different properties of the two compared subsamples. For example, the first line compares the (low-z and $M_r < -15.2$ mag and $R \leqslant 0.5\,R_{200}$) subsample and (low-z and $M_r < -15.2$ mag and $0.5\,R_{200} < R \leqslant R_{200}$) subsample, deriving the K-S test $p = 8.2 \times 10^{-1}$; the last line compares the ($R \leqslant R_{200}$ and $M_r > -15.2$ mag and low-z) subsample and ($R \leqslant R_{200}$ and $M_r > -15.2$ mag and intermediate-z) subsample, deriving the K-S $p = 1.8 \times 10^{-1}$.

Table 3
MCMC Results of Intrinsic Morphology Analysis for the Different Samples of Low-z and Intermediate-z UDGs

Redshift	UDG Samples	N	$\bar{E}$	σ_E	$\bar{T}$	σ_T	A:B:C
	All (Sample 1+2+3)	1109	$0.51^{+0.01}_{-0.02}$	$0.12^{+0.02}_{-0.01}$	$0.34^{+0.22}_{-0.05}$	$0.21^{+0.15}_{-0.08}$	1:0.86:0.49
	Sample 1	328	$0.49^{+0.01}_{-0.01}$	$0.12^{+0.02}_{-0.01}$	$0.34^{+0.20}_{-0.09}$	$0.22^{+0.37}_{-0.12}$	1:0.86:0.51
	Sample 2	442	$0.52^{+0.01}_{-0.02}$	$0.11^{+0.02}_{-0.01}$	$0.35^{+0.41}_{-0.13}$	$0.29^{+0.38}_{-0.17}$	1:0.85:0.48
	Sample 3	339	$0.49^{+0.01}_{-0.02}$	$0.12^{+0.02}_{-0.01}$	$0.36^{+0.41}_{-0.20}$	$0.50^{+0.31}_{-0.27}$	1:0.86:0.51
	$R \leqslant 0.5\,R_{200}$	471	$0.48^{+0.01}_{-0.01}$	$0.12^{+0.01}_{-0.01}$	$0.37^{+0.29}_{-0.12}$	$0.36^{+0.37}_{-0.19}$	1:0.85:0.52
	$0.5\,R_{200} < R \leqslant R_{200}$	443	$0.50^{+0.01}_{-0.02}$	$0.12^{+0.02}_{-0.01}$	$0.35^{+0.38}_{-0.15}$	$0.38^{+0.36}_{-0.20}$	1:0.86:0.50
	$R > R_{200}$	195	$0.57^{+0.02}_{-0.02}$	$0.22^{+0.02}_{-0.01}$	$0.37^{+0.55}_{-0.18}$	$0.39^{+0.38}_{-0.34}$	1:0.84:0.43
Low-z UDGs	$R \leqslant 0.2\,R_{200}$	96	$0.47^{+0.01}_{-0.02}$	$0.12^{+0.03}_{-0.02}$	$0.29^{+0.09}_{-0.07}$	$0.06^{+0.22}_{-0.05}$	1:0.89:0.53
	$M_r < -15.2$	543	$0.49^{+0.01}_{-0.01}$	$0.12^{+0.01}_{-0.01}$	$0.35^{+0.14}_{-0.08}$	$0.24^{+0.37}_{-0.10}$	1:0.86:0.51
	$M_r > -15.2$	566	$0.52^{+0.01}_{-0.01}$	$0.11^{+0.01}_{-0.01}$	$0.33^{+0.21}_{-0.15}$	$0.37^{+0.34}_{-0.18}$	1:0.86:0.48
	$M_r < -15.2$ and $R \leqslant 0.5\,R_{200}$	230	$0.45^{+0.02}_{-0.02}$	$0.13^{+0.03}_{-0.02}$	$0.38^{+0.51}_{-0.18}$	$0.34^{+0.38}_{-0.29}$	1:0.86:0.55
	$M_r < -15.2$ and $0.5\,R_{200} < R \leqslant R_{200}$	216	$0.45^{+0.02}_{-0.02}$	$0.14^{+0.03}_{-0.02}$	$0.67^{+0.22}_{-0.29}$	$0.34^{+0.36}_{-0.26}$	1:0.73:0.55
	$M_r < -15.2$ and $R > R_{200}$	97	$0.51^{+0.02}_{-0.03}$	$0.12^{+0.03}_{-0.02}$	$0.36^{+0.55}_{-0.16}$	$0.17^{+0.47}_{-0.15}$	1:0.85:0.49
	$M_r > -15.2$ and $R \leqslant 0.5\,R_{200}$	241	$0.51^{+0.02}_{-0.02}$	$0.11^{+0.02}_{-0.01}$	$0.44^{+0.32}_{-0.10}$	$0.28^{+0.38}_{-0.15}$	1:0.82:0.49
	$M_r > -15.2$ and $0.5\,R_{200} < R \leqslant R_{200}$	227	$0.54^{+0.02}_{-0.02}$	$0.10^{+0.02}_{-0.02}$	$0.27^{+0.26}_{-0.14}$	$0.26^{+0.29}_{-0.20}$	1:0.89:0.46
	$M_r > -15.2$ and $R > R_{200}$	98	$0.65^{+0.02}_{-0.02}$	$0.04^{+0.02}_{-0.02}$	$0.56^{+0.36}_{-0.21}$	$0.34^{+0.37}_{-0.26}$	1:0.71:0.35
Intermediate-z UDGs	All (Sample 4)	84	$0.54^{+0.02}_{-0.02}$	$0.07^{+0.03}_{-0.02}$	$0.40^{+0.05}_{-0.05}$	$0.02^{+0.07}_{-0.02}$	1:0.83:0.46

Note. Column (1): low-z or intermediate-z UDG sample. Column (2): UDG sample with the different properties. Column (3): number of UDGs in each sample used for MCMC. Columns (4)–(7): mean values and standard deviations of ellipticity and triaxiality distributions $\bar{E}$, σ_E, $\bar{T}$, and σ_T. Column (8): median ratios of three intrinsic axes A:B:C.

over nearly prolate ones.[23] The discovery of the triaxial UDG morphologies is consistent with the hydrodynamical simulation results (e.g., Jiang et al. 2019) but in conflict with the conclusion of Burkert (2017). This conflict is due to the fact that Burkert (2017) only compared the purely oblate and purely prolate models, while in nature there is no a priori reason for preferring either of these extremes.

The intrinsic axis ratios, C/A and B/A, are then calculated from $\bar{E}$, σ_E, $\bar{T}$, and σ_T. Since $E \sim 0.5$–0.6 and $T \sim 0.3$–0.4, we find $C/A \sim 0.4$–0.5 and $B/A \sim 0.8$–0.9, suggesting that the intrinsic morphologies of cluster UDGs actually are "oblate-triaxial" ($C/B < B/A$).

In order to study the shape dependence on luminosities, environments, and redshifts, we also implement the MCMC method to analyze the intrinsic morphologies of the UDG subsamples with the different properties and show the results in

[23] We also note that, in theory, one can alternatively assume that one UDG sample is made up of two divergent populations with $\bar{T} \sim 0.3$–0.4 and $\bar{T} \sim 1.0$, respectively; however, we prefer a simpler model with only one set of ellipticity and triaxiality parameters to describe the intrinsic morphology of cluster UDGs in one sample, particularly in the case in which the triaxial model alone can well recover the q distributions of UDGs.

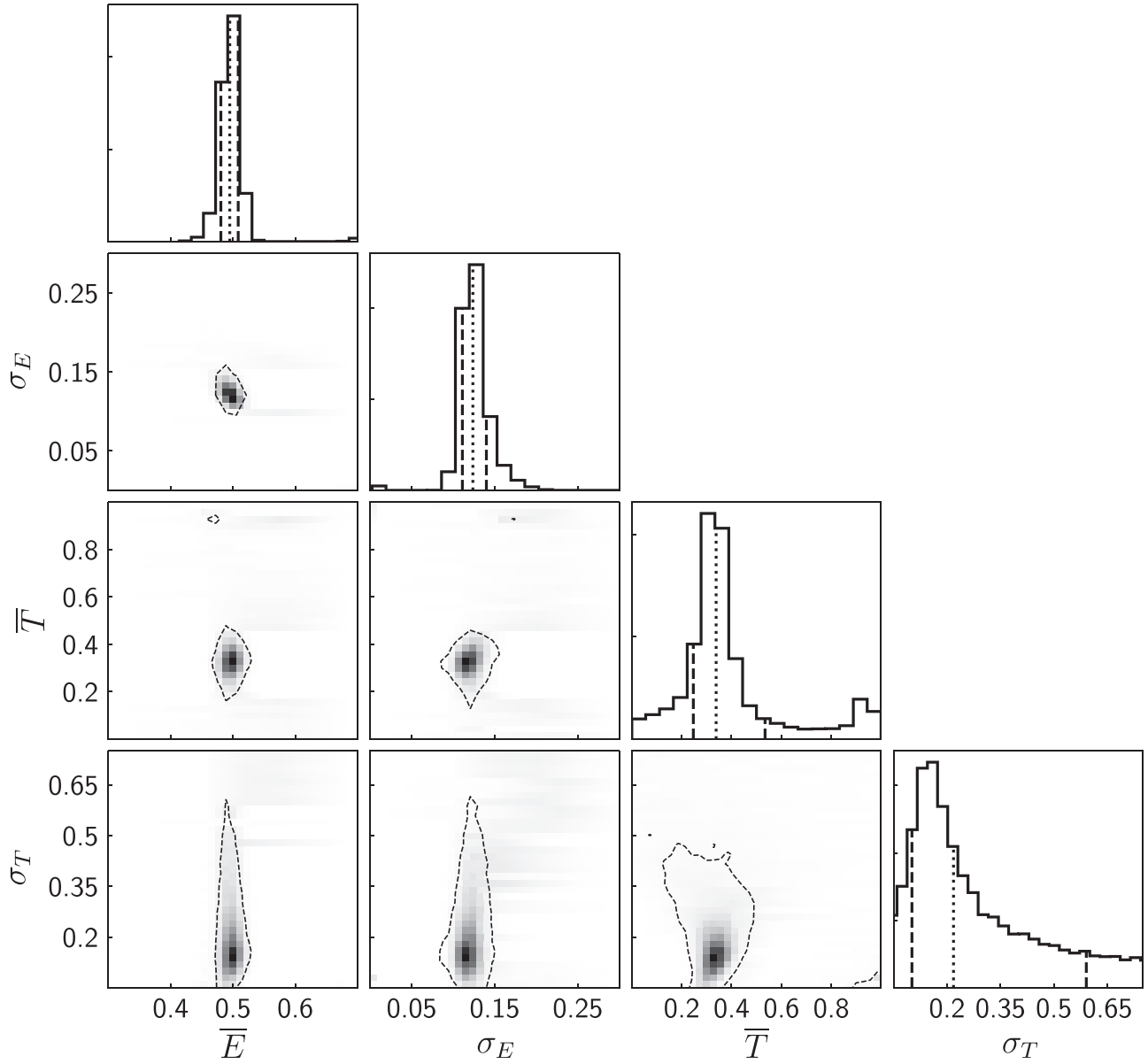

Figure 5. Posterior pdf's of $\bar{E}$, σ_E, $\bar{T}$, and σ_T for sample 1 of low-z UDGs in the Coma Cluster. The panels in the diagonal show the posterior pdf's for each of the parameters, marginalized over all the other ones. The gray scale in the nondiagonal panels shows the corresponding joint posterior pdf's. Contours enclose the regions that contain 68% of the cumulative posterior probability. The dashed, dotted, and dashed lines (left to right) in the diagonal panels indicate 16%, 50%, and 84% of the corresponding marginalized posteriors.

Table 3. Since, compared with the ellipticity distributions, the triaxiality distributions are worse constrained with photometric data alone (Binggeli 1980), analogous to the work of Sánchez-Janssen et al. (2019), we will therefore focus our analysis on the comparison of galaxy flattenings ($\bar{E}$) and thicknesses ($\bar{C/A}$).

3.2. UDG Morphology Evolution with Masses

As listed in Table 3, the intrinsic morphologies of the high-mass and low-mass low-z UDGs are significantly different, regardless of their environments. In the top panel of Figure 9, we compare the median intrinsic thickness, $\bar{C/A}$, for the high-mass and low-mass UDGs located in $R \leqslant 0.5\,R_{200}$ (red), $0.5\,R_{200} < R \leqslant R_{200}$ (yellow), and $R > R_{200}$ (blue), respectively. We find that (1) for the UDGs located in the same environment, the high-mass ones are always thicker, puffier, than the low-mass ones (see also Appendix B); and (2) the morphology difference between the high-mass and low-mass ones is present in both $R < R_{200}$ and $R > R_{200}$.

Since the thickness difference between the high-mass and low-mass UDGs always exists in the different environments, it may originate from internal processes, e.g., supernova feedback. Star formation in dwarf galaxies is expected to occur in episodic bursts at almost all redshifts (Muratov et al. 2015), and the associated supernova-driven outflows pressurize gas and heat[24] the stellar orbits (Governato et al. 2010; Pontzen & Governato 2012; Teyssier et al. 2013; El-Badry et al. 2016). If UDGs are proposed to be produced by outflows (e.g., Di Cintio et al. 2017), as a consequence of more starbursts or a larger

[24] Multiple supernova explosions induce strong and repeated fluctuations in the dwarf gravitational potential, which result in energy transfer to the collisionless components (dark matter and stars).

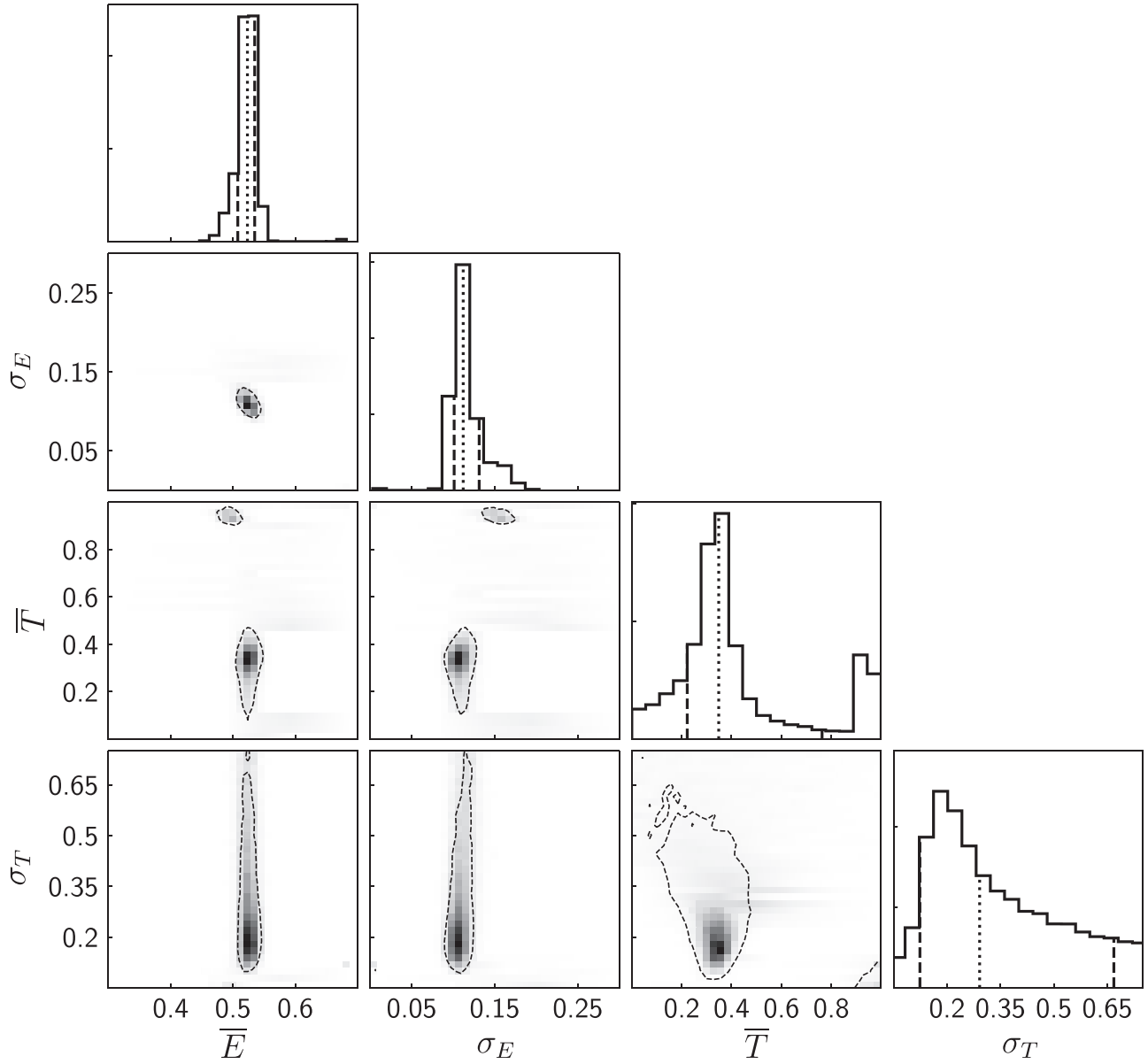

Figure 6. Analogous to Figure 5, posterior pdf's of $\bar{E}$, σ_E, $\bar{T}$, and σ_T for sample 2 of low-z UDGs in eight nearby clusters.

amount of star formation, the higher-mass UDGs should have delivered more energy to heat up the stellar random motions and thus become less flattened.

Galaxy merging can also lead to morphological transformation (e.g., Starkenburg et al. 2016a, 2016b) and simultaneously starbursts, which can significantly boost stellar mass assembly. However, many simulations and observational results have excluded mergers from playing any significant role in determining the morphologies of dwarf galaxies (e.g., Stewart et al. 2008; Rodriguez-Gomez et al. 2015, 2017), as the mergers of dwarf galaxies are very rare.

Although direct mergers are extremely rare, the rate of tidal encounters with more massive galaxies during flybys (including "harassment" and tidal stirring; Moore et al. 1996; Mayer et al. 2001, 2007) is considerable, particularly in the massive clusters comprising many massive satellites. The tidal interactions can also efficiently puff up UDGs and transform the kinematic and stellar distributions to resemble the present-day dE/dSphs (e.g., Moore et al. 1996; Mayer et al. 2001; Errani et al. 2015; Carleton et al. 2019). In simulations, the stellar dispersions in cluster UDGs with more massive remnant stellar masses after tidal interactions are found to be higher than those in lower-mass counterparts (see Carleton et al. 2019), plausibly explaining the thicker galactic bodies of the higher-mass UDGs as shown in the top panel of Figure 9.

Sánchez-Janssen et al. (2019) found that the morphologies of typical quiescent dwarf galaxies, populating the RS, also depend on galaxy luminosities. We therefore compare the UDG thickness dependence on luminosity with that of the quiescent dE/dSphs located in the nearby Virgo and Fornax Clusters (Sánchez-Janssen et al. 2019) and in the Local Group (McConnachie 2012) and Centaurus A galaxy group (Taylor et al. 2017, 2018)[25], as well as trends of massive early-type galaxies (ETGs) and late-type galaxies (LTGs) selected from

[25] The r-band absolute magnitudes of the dE/dSphs in the Virgo and Fornax Clusters and the Centaurus A group are obtained by assuming $g - r \sim 0.6$ (e.g., Rong et al. 2017a; Venhola et al. 2018), while the magnitudes of the dwarfs in the Local Group are directly found in McConnachie (2012).

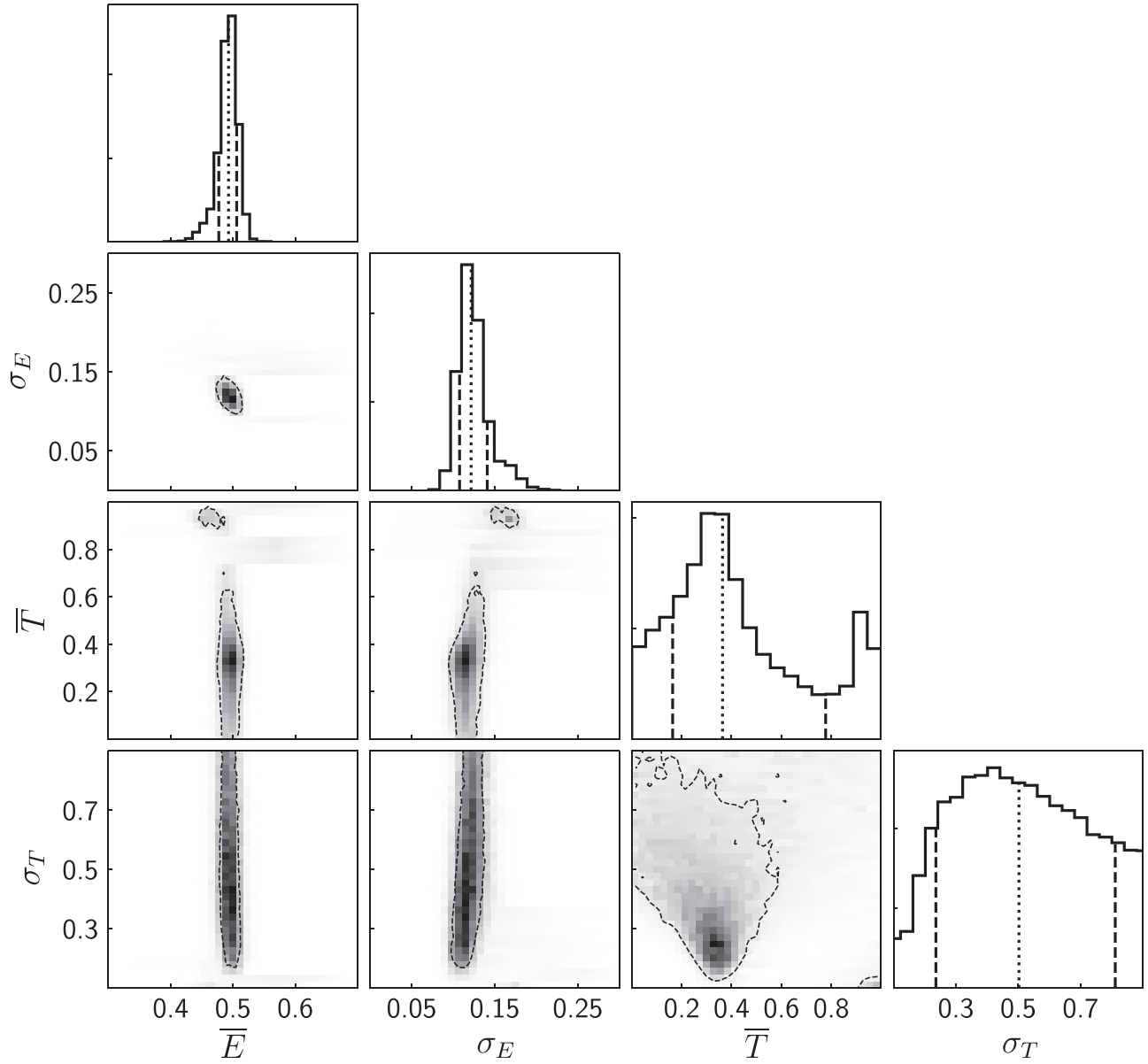

Figure 7. Analogous to Figure 5, posterior pdf's of $\bar{E}$, σ_E, $\bar{T}$, and σ_T for sample 3 of low-z UDGs in eight nearby clusters.

the Sloan Digital Sky Survey data sets (Padilla & Strauss 2008; Rodríguez & Padilla 2013). As shown in the top panel of Figure 9, the thickness trend of the low-z cluster UDGs with luminosities (the gray shaded region) is apparently contrary to the trend of the typical quiescent dE/dSphs[26] in nearby clusters and groups (the yellow shaded region; see also Sánchez-Janssen et al. 2019) but is "akin to" the trends of massive ETGs (the dark-green shaded region) and LTGs[27] (the light-green shaded region). Note that the trend (yellow shaded region) of typical dE/dSphs is believed to be caused by the lower binding energies of the fainter dwarfs (see, e.g., Sánchez-Janssen et al. 2019); the different trends of UDGs and typical dE/dSphs may imply that the violent internal or external processes, such as stellar feedback or tidal interaction, play a much more crucial role in the evolution of UDGs, compared with the typical dE/dSphs. In this sense, UDGs may not be simply treated as an extension of the dE/dSph class with similar evolutionary histories; they may differ not only in size.

3.3. UDG Morphology Evolution with Environments

In the bottom panel of Figure 9, we show the median intrinsic thickness as a function of R/R_{200} for the entire (black), high-mass (red), and low-mass (blue) low-z UDG samples. From $R > R_{200}$ to $R < R_{200}$, UDGs become significantly puffed up; this outside-in evolution is stronger for lower-mass systems. However, in the virial radii of clusters, the thicknesses of UDGs only mildly increase with decreasing R/R_{200},

[26] The thicknesses of the bright and faint dwarfs in Sánchez-Janssen et al. (2019) are obtained from $C/A = (C/A_{\rm nuc}{}^{*}N_{\rm nuc} + C/A_{\rm non}{}^{*}N_{\rm non})/N_{\rm tot}$, where $C/A_{\rm nuc}$, $C/A_{\rm non}$ denote the thicknesses of the nucleated and non-nucleated dwarfs in each sample, respectively, and $N_{\rm nuc}$, $N_{\rm non}$, $N_{\rm tot}$ denote the number of the nucleated, non-nucleated, and entire sample of dwarfs, respectively.

[27] There is also literature discussing that the fainter LTGs, with absolute magnitudes of $M_g > -18$ mag, again show thicker morphologies as they get fainter (e.g., Sánchez-Janssen et al. 2010; Roychowdhury et al. 2013); however, in this work we only focus on the morphology trend for the massive LTGs with $M_g < -18$ mag.

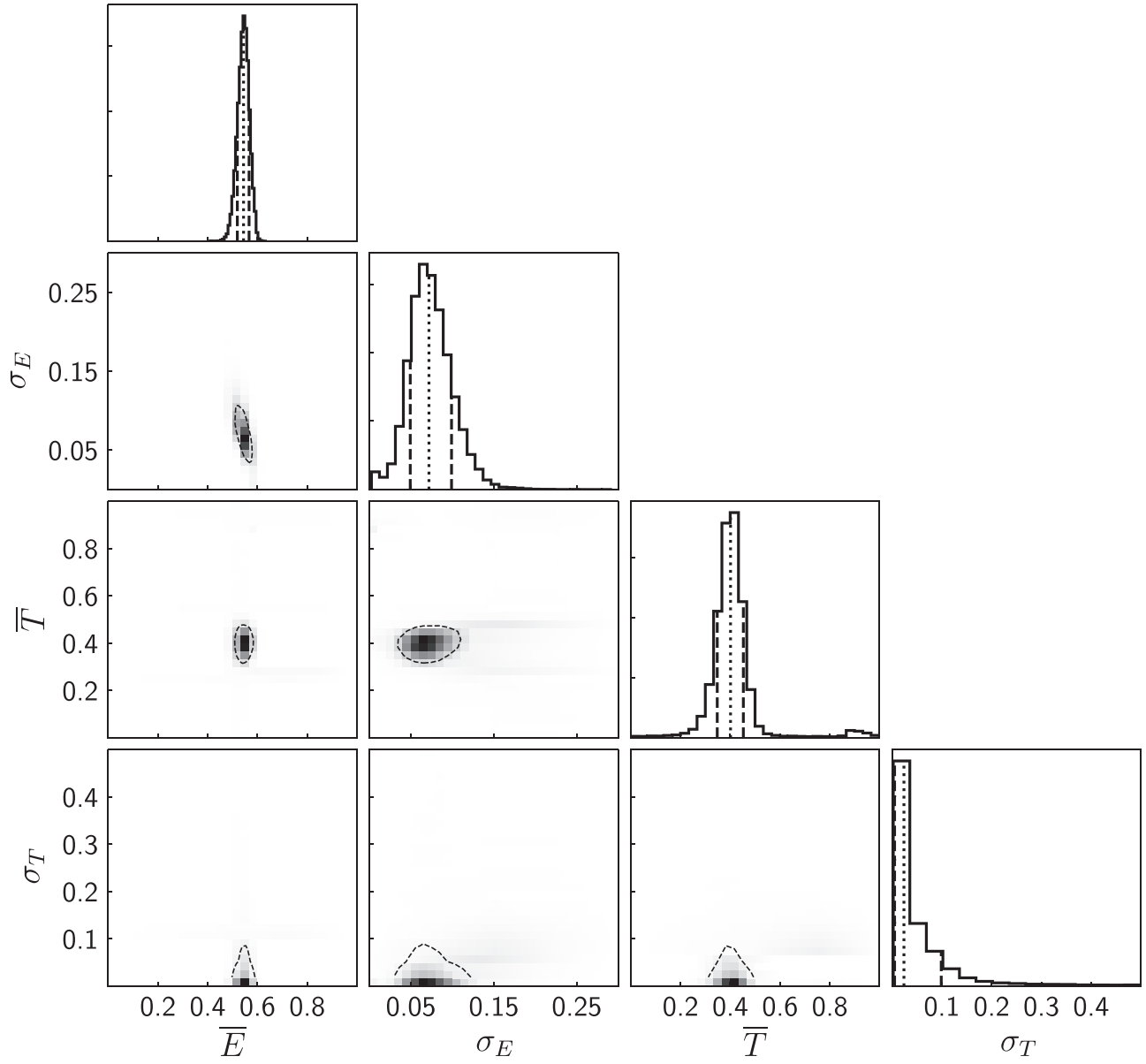

Figure 8. Analogous to Figure 5, posterior pdf's of $\bar{E}$, σ_E, $\bar{T}$, and σ_T for sample 4 of intermediate-z UDGs in A2744 and AS1063.

consistent with the relatively high p values from the K-S tests as shown in Table 2. These results suggest a prominent environmental effect on morphological transformation of UDGs from outside to inside of R_{200}, but probably a weak environmental effect for the ones moving in clusters.

As discussed in Section 3.2, tidal interactions may be responsible for the puffed-up morphologies of UDGs in the denser environments; meanwhile, tidal interactions also extend sizes of UDGs (e.g., Errani et al. 2015; Carleton et al. 2019). In particular, UDGs embedded in cored halos expand much more significantly after tidal interactions, compared with the cuspy counterparts; however, the stellar mass within half-light radius is not significantly altered by the stripping process for the UDGs in cored halos (see Carleton et al. 2019). Since tidal influences are more prominent in higher-density environments (i.e., smaller R/R_{200}), we should therefore expect the sizes of stellar components to change with R/R_{200} but luminosities to remain roughly constant. As shown by the M_r and r_e (the median value and 1σ scatter are shown by the solid and dashed components, respectively) as functions of R/R_{200}[28] in Figure 10, the sizes r_e for both the high-mass and low-mass UDGs indeed slightly increase with decreasing R/R_{200}, while there is no obvious radial gradient in luminosity among our low-z UDG samples.

We note that a large/dominant fraction of the present-day cluster UDGs might not be accreted as UDGs (Alabi et al. 2018; Ferré-Mateu et al. 2018) but be transformed from typical dwarf progenitors under tidal interactions in clusters (e.g., Jiang et al. 2019; Liao et al. 2019); these "in situ transformed" UDGs may weaken the averaged radial trends of r_e and morphological transformation of UDGs.

[28] Since Sample 3 applies a more conservative selection criterion of $r_{e,c} = r_e\sqrt{q} > 1.5$ kpc (slightly different from the standard criterion $r_e > 1.5$ kpc for Samples 1 and 2), and Sample 3 UDGs are only located in $R < R_{200}$; therefore, in order to show the unbiased trends, we only show the radial trends for the low-z UDGs with $r_{e,c} > 1.5$ kpc.

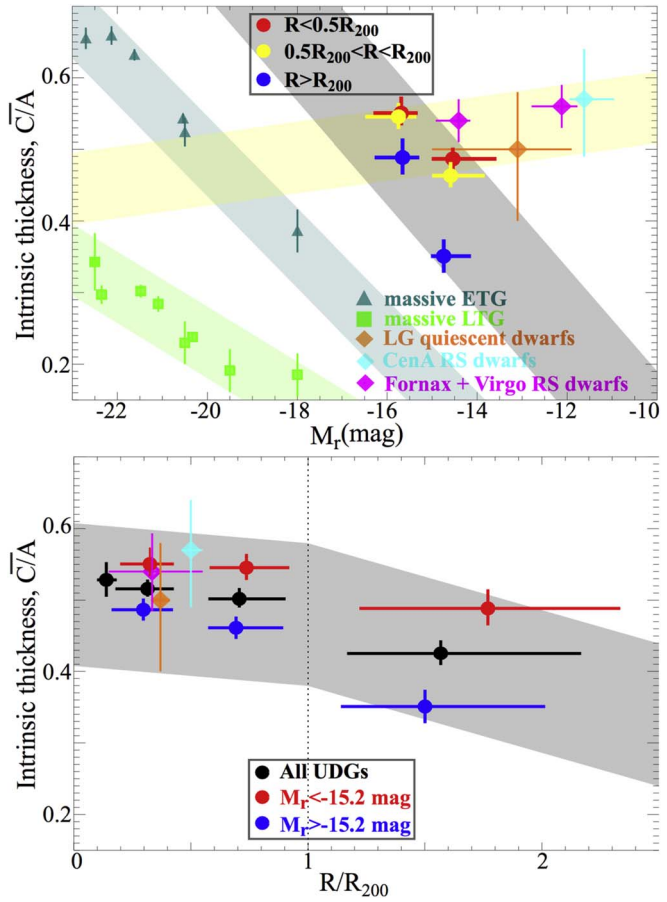

Figure 9. Median intrinsic thickness $\bar{C/A}$ as a function of luminosity (top panel) and R/R_{200} (bottom panel) for our low-z UDG samples. In the two panels, the filled circles denote all UDGs, high-mass UDGs, and low-mass UDGs, respectively. In the top panel, the red, yellow, and blue filled circles denote the UDGs located in $R \leqslant 0.5\,R_{200}$, $0.5\,R_{200} < R \leqslant R_{200}$, and $R > R_{200}$, respectively. In the bottom panel, the black, red, and blue filled circles denote the all, high-mass, and low-mass UDGs, respectively, and the vertical dotted line denotes the virial radius of $R = R_{200}$. For comparison, we also plot the thicknesses of quiescent dE/dSphs that follow the red sequence in nearby clusters (Virgo+Fornax, magenta diamond; Sánchez-Janssen et al. 2019) and groups (Local Group, orange; Centaurus A, cyan; McConnachie 2012; Taylor et al. 2017, 2018; Sánchez-Janssen et al. 2019), as well as massive ETGs (dark-green triangles) and LTGs (light-green triangles) selected from the Sloan Digital Sky Survey catalog by Padilla & Strauss (2008) and Rodríguez & Padilla (2013). The gray shaded regions show the thickness trends for the UDG samples with the different luminosities and located in the different environments; the dark- and light-green shaded regions highlight the corresponding thickness trends for the massive ETGs and LTGs within the different luminosity ranges, respectively; the yellow shaded region reveals the thickness trend for the dE/dSphs with the different luminosities in nearby clusters and groups shown by Sánchez-Janssen et al. (2019). The slopes of the plotted gray shaded trends are derived from linear fitting to the point pairs corresponding to the same environments (top panel) or same mass ranges (bottom panel); it is worth noting that the quantitative slopes are not crucial in this work, as there are large uncertainties.

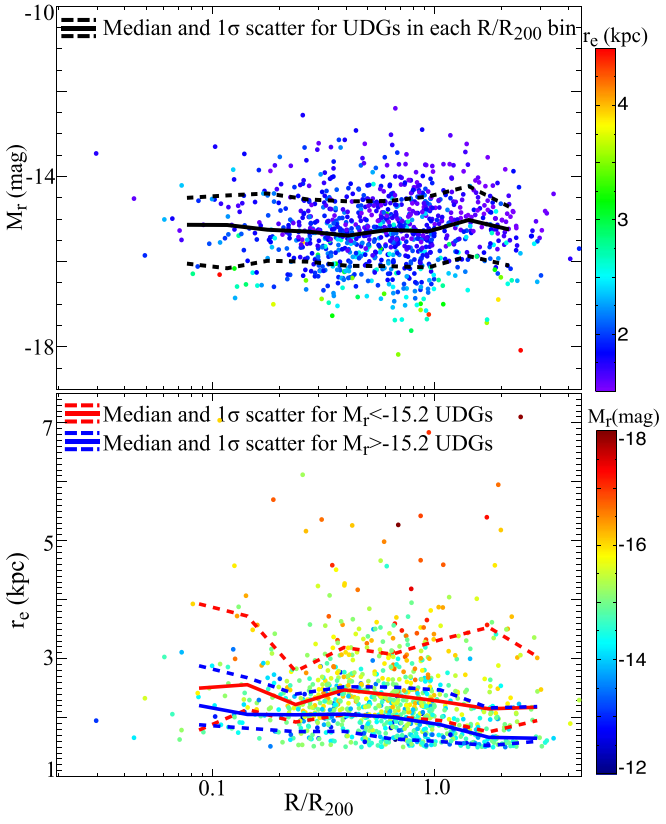

Figure 10. Luminosities (top panel) and UDG sizes (bottom panel) as functions of R/R_{200}. In the top panel, the different colored dots denote the low-z UDGs with the different effective radii; the solid and dashed components show the median and 1σ scatter of UDG luminosities in each R/R_{200} bin, respectively. In the bottom panel, the different colored dots denote the low-z UDGs with the different M_r; the solid and dashed components show the median and 1σ scatter of UDG sizes in each R/R_{200} bin for the high-mass (red) and low-mass (blue) subsamples, respectively. We only plot the results for the conservative sample of UDGs with $r_{e,c} > 1.5$ kpc.

Apart from the contamination of the "in situ transformed" cluster UDGs, the less efficient "environmental quenching" (e.g., ram pressure/tidal stripping or "strangulation"; Larson et al. 1980; Moore et al. 1996; Read & Gilmore 2005; Mayer et al. 2007; Kawata & Mulchaey 2008; Bekki 2009; Arraki et al. 2014) may also reconcile the pronounced thickening of UDGs from $R > R_{200}$ to $R < R_{200}$, but mild thickening from $R \lesssim R_{200}$ to $R \sim 0$. In this scenario, the environmental quenching timescale may be relatively long (Wheeler et al. 2014), so that the recently accreted UDGs, primarily occupying the peripheries of clusters, may continue to retain their gas reservoirs, which cause galaxies to respond more impulsively to tides, significantly augmenting their morphological transformation (Kazantzidis et al. 2017). However, most of the inner-region UDGs are devoid of gas, and thus their morphological transformation becomes less efficient, compared with the outer-region counterparts.

Another possibility is the contamination of interlopers. The UDG samples are selected based on their locations in the color–magnitude diagrams and may include a fraction of reddened background massive star-forming interlopers. The contamination is more significant in the projected "outer regions" of clusters, where the clusters become less overdense and comprise member galaxies with larger color scatters (e.g., Lee & Jang 2016; van der Burg et al. 2016; Lee et al. 2017); therefore, these disky interlopers with small thicknesses, primarily located in the outer regions of clusters, can introduce a more significant thickening of "UDGs" from $R > R_{200}$ to $R < R_{200}$.

In addition, the mild radial trend in R_{200} may be partly attributed to projection effects, i.e., the so-called "inner-region" ($R < 0.5R_{200}$) UDG population may actually contain many projected middle/outer-region UDGs.

3.4. UDG Morphology Evolution with Redshifts

The morphological transformation of UDGs from the intermediate to low redshift is also investigated. Since only ~7% of the intermediate-z UDGs are located beyond R_{200}, the intermediate-z UDGs can be roughly treated as a cluster-UDG

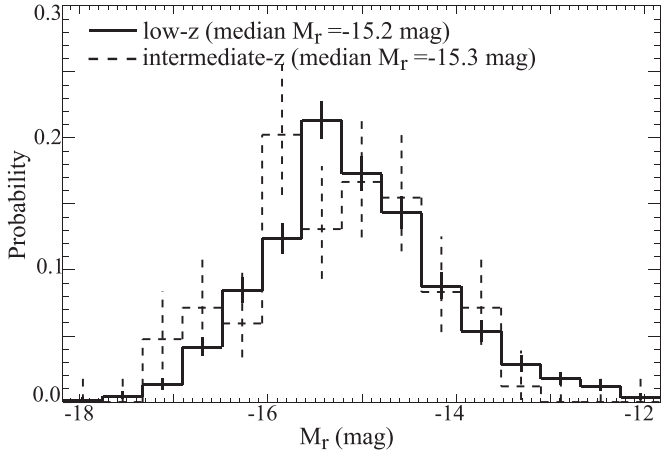

Figure 11. Distributions of M_r for the low-z samples located in $R < R_{200}$ and the intermediate-z sample.

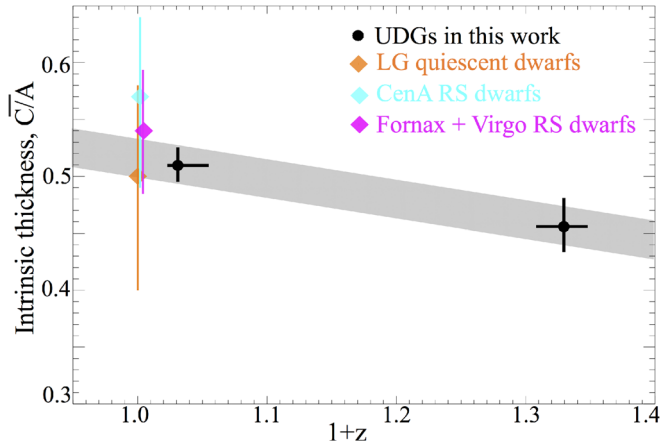

Figure 12. Median intrinsic thickness $\bar{C}/A$ as a function of redshift for UDGs in this work (black), and dE/dSphs in the Local Group (orange; McConnachie 2012) and Centaurus A galaxy group (cyan; Taylor et al. 2017, 2018), as well as dE/dSphs in the nearby clusters of Virgo and Fornax (magenta; Sánchez-Janssen et al. 2019). The gray shaded region shows the thickness trend for the UDGs located at the different redshifts. Analogous to Figure 9, the slope of the gray shaded trend is derived from linear fitting to the two black filled circles.

sample; besides, as shown in Figure 11, the luminosities of the intermediate-z UDG sample and low-z $R \leqslant R_{200}$ sample are approximately in the same M_r range, with a median M_r value of -15.3 and -15.2 mag, respectively. Therefore, the intermediate-z UDG sample can be directly compared with the low-z $R \leqslant R_{200}$ UDG sample.

As explored in Figure 12, the median intrinsic thickness of cluster UDGs slightly increases from intermediate to low redshift, probably suggesting that the cluster UDGs are marginally puffed up from $z \sim 0.35$ to 0. Therefore, naively, we can suspect that the high-redshift, initial UDGs may be more flattened, and plausibly have a "disky" morphology. If we treat these intermediate-z UDGs as the progenitors of the present-day cluster UDGs, it may imply that UDGs originated from a formation mechanism (e.g., high-spins of halos; Amorisco & Loeb 2016; Rong et al. 2017a), which can produce the "disky" morphologies in the first place.

Here, we also point out that the morphology difference between the high- and low-redshift UDGs may be driven by the small UDG sample from two intermediate-z clusters, and thus the morphological transformation trend has large uncertainties and requires further confirmation with larger intermediate-z UDG samples.

4. Summary and Discussion

With the data of apparent axis ratios for 1109 UDGs located in 17 low-z ($z \sim 0.020$–0.063) galaxy clusters and 84 UDGs in two intermediate-z ($z \sim 0.308$–0.348) clusters, we implement an MCMC technology and assume a triaxial model to study the intrinsic morphologies of UDGs. In contrast to the conclusion of Burkert (2017), we emphasize that the UDG data favor the oblate-triaxial models over purely prolate models.

The morphologies of UDGs are related to luminosity, environment, and redshift. For the low-z UDGs, the ones with higher masses or located inside of the virial radii of clusters are significantly puffed up, compared with the counterparts with low masses or located outside of the virial radii of clusters. Considering together the UDG morphologic dependences on luminosity and environment, we conclude that the most possible physical mechanism of leading to both morphologic dependences is tidal interaction, essentially agreeing with the previous conclusion in, e.g., Conselice (2018), though we cannot exclude that stellar feedback may also play a role in the UDG morphologic dependence on luminosity.

Note that the UDG thickness dependence on luminosity is distinct from that of the typical quiescent dE/dSphs in nearby clusters and groups, suggesting that tidal interaction plays a much more crucial role in the evolution of UDGs compared with the typical dwarfs. It probably implies that UDGs may not be simply treated as an extension of the dE/dSph class with similar evolutionary histories; they may differ not only in size.

From intermediate to low redshift, the morphologies of cluster UDGs become marginally puffier and have broader ranges of ellipticity and triaxiality, plausibly suggesting a formation mechanism producing "disky" morphologies for the high-redshift, newly born UDG progenitors, e.g., being formed in the high specific angular momentum halos (Amorisco & Loeb 2016; Rong et al. 2017a). However, the number of UDGs at relatively high redshifts is small; we strongly encourage further high spatial resolution, deep surveys for high-redshift UDGs to examine this conclusion.

Note that tidal interactions can alleviate the tension between the detected high specific angular momenta of the field UDGs (Leisman et al. 2017) and large dispersion or no signs for rotation in cluster UDGs (e.g., van Dokkum et al. 2016; Chilingarian et al. 2019; Danieli et al. 2019): the high-redshift, rotationally supported, field UDGs (resembling present-day dwarf irregulars) might originate in the halos with high specific angular momenta and have initial shapes with relatively small thicknesses; when UDGs were accreted to high-density environments, the tidal interactions can efficiently reduce their angular momenta and transform UDG morphologies, to make their two-dimensional morphologies resemble dEs, dS0s, and dSphs (Zabludoff & Mulchaey 1998; Cortese et al. 2006; McGee et al. 2009; De Lucia et al. 2012; Peng et al. 2012; Vijayaraghavan & Ricker 2013; Rong et al. 2015b, 2016; Vijayaraghavan et al. 2015; Alabi et al. 2018; Ferré-Mateu et al. 2018).

We thank the referee for her/his helpful comments and suggestion. We acknowledge the publicly available UDG catalogs in Yagi et al. (2016) and Lee et al. (2017). Y.R. acknowledges the helpful comments and suggestions from M. G. Lee, R. Sánchez-Janssen, L. Gao, Q. Guo, S.-H. Liao, and J. Wang, as well as funding support from FONDECYT Postdoctoral Fellowship Project No. 3190354 and NSFC grant No. 11703037. T.H.P. acknowledges support through FONDECYT

Regular project 1161817 and CONICYT project Basal AFB-170002. H.-X.Z. acknowledges support from the CAS Pioneer Hundred Talents Program and the NSFC grant 11421303. This work is also supported by CAS South America Center for Astronomy (CASSACA), Chinese Academy of Sciences (CAS).

This research has made use of the NASA Astrophysics Data System Bibliographic Services, the NASA Extragalactic Database, PYTHON/EMCEE v.2.2.1 (Foreman-Mackey et al. 2013, https://emcee.readthedocs.io/en/v2.2.1/) package, GALFIT (Peng et al. 2002, 2010), and ds9 (a tool for data visualization supported by the Chandra X-ray Science Center and the High Energy Astrophysics Science Archive Center with support from the James Webb Space Telescope Mission office at the Space Telescope Science Institute for 3D visualization). We also acknowledge the related literature of Goodman & Weare (2010), Jones et al. (2001), Rong et al. (2017b, 2018b), Astropy Collaboration et al. (2013), and Hunter (2007).

Appendix A
MCMC Results versus Observations

In this appendix, we test whether the MCMC results are robust and can well recover the observed q distributions of UDGs. Particularly for the low-z samples, the $\bar{T}$ posterior pdf's actually contain two peaks (local maximum likelihood) overlapping at about $\bar{T} \simeq 0.8$ (see Figures 5–7; the primary peak at $\bar{T} \sim 0.3 - 0.4$ and secondary peak at $\bar{T} \sim 1.0$), and the posterior pdf's of $\bar{T} < 0.8$ resembling Gaussian distribution correspond to the triaxial models, while posterior pdf's of $\bar{T} > 0.8$ suggest the nearly prolate models.

It is worth noting that, in MCMC, these $\bar{T} > 0.8$ steps are not "burn-in" steps that should be discarded. Indeed, the MCMC chain converges to an equilibrium distribution after approximately 200 "burn-in" steps (Sánchez-Janssen et al. 2016), and we actually apply "nburn" = 400 in the affine-invariant MCMC algorithm implemented in the Python EMCEE package (Foreman-Mackey et al. 2013). We also set "nburn" = 500, 1000, 2000, and 4000 (with the other parameters remaining unchanged) and find that the $\bar{T}$ posterior pdf's of the low-z samples always show double peaks.

Further, as shown in Figure A1, we find that both the triaxial models and nearly prolate models generated from MCMC can well recover the observed q distributions.[29] In summary, the MCMC results are robust and the $\bar{T} > 0.8$ steps are not "burn-in" steps.

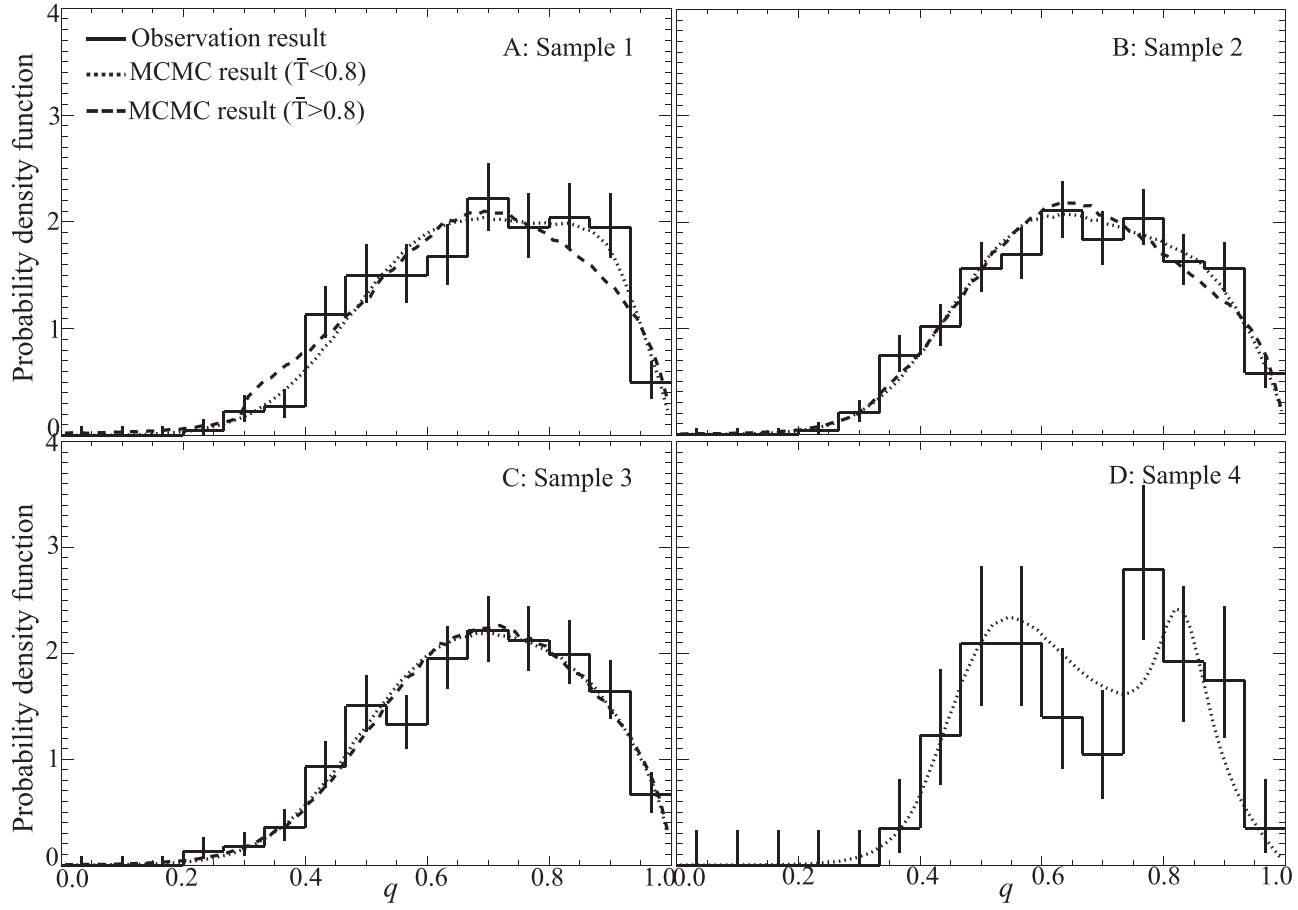

Figure A1. Comparison between the observational q distributions (solid histograms) and recovered distributions by the triaxial models (with the sets of $(\bar{E}, \sigma_E, \bar{T}, \sigma_T)$ corresponding to $\bar{T} < 0.8$; dotted) and purely prolate models (with the sets of $(\bar{E}, \sigma_E, \bar{T}, \sigma_T)$ corresponding to $\bar{T} > 0.8$; dashed), derived from MCMC, for the four UDG samples.

[29] Actually, compared with the nearly prolate models, the triaxial models can reproduce the marginally flatter q distributions in the range of $q \sim 0.6$–0.9, more closely resembling the observed q distributions, as shown in Figure A1.

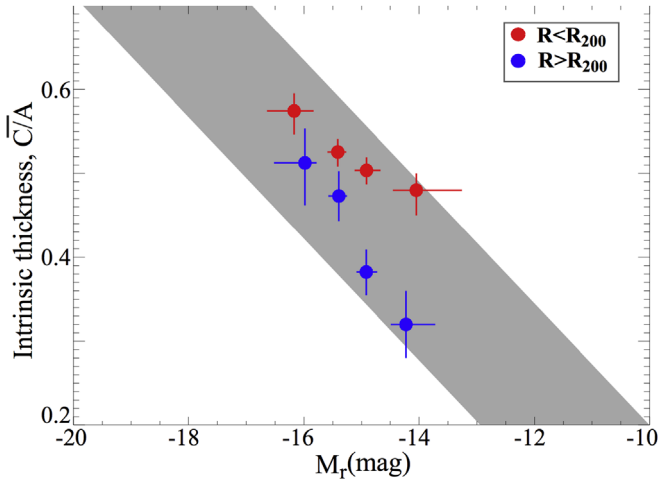

Figure B1. Thickness of UDGs as a function of absolute magnitudes. The red and blue filled circles denote the UDGs in and out of R_{200}, respectively. Analogous to Figure 9, the gray shaded region shows the UDG thickness trend that the more luminous UDGs show puffier morphologies.

Appendix B
UDG Morphologic Dependence on Luminosity

In this appendix, for the low-z UDGs, we split both the R_{200} and $R > R_{200}$ samples into four subsamples (instead of the two subsamples with $M_r < -15.2$ mag and $M_r > -15.2$ mag) according to their absolute magnitudes, to retest the UDG thickness dependence on luminosity. As shown in Figure B1, we can still find the significant decreasing trend of UDG thicknesses with the decreasing luminosities, though the uncertainties of thicknesses of UDGs are relatively large.

ORCID iDs

Yu Rong https://orcid.org/0000-0002-2204-6558
Xiao-Yu Dong https://orcid.org/0000-0002-4002-861X
Thomas H. Puzia https://orcid.org/0000-0003-0350-7061
Gaspar Galaz https://orcid.org/0000-0002-8835-0739
Ruben Sánchez-Janssen https://orcid.org/0000-0003-4945-0056
Tianwen Cao https://orcid.org/0000-0002-1335-6212
Cristóbal Sifón https://orcid.org/0000-0002-8149-1352
Pavel E. Mancera Piña https://orcid.org/0000-0001-5175-939X
Giuseppe D'Ago https://orcid.org/0000-0001-9697-7331
Hong-Xin Zhang https://orcid.org/0000-0003-1632-2541
Evelyn J. Johnston https://orcid.org/0000-0002-2368-6469
Paul Eigenthaler https://orcid.org/0000-0001-8654-0101

References

Aguerri, J. A. L., & González-García, A. C. 2009, A&A, 494, 891
Alabi, A., Ferré-Mateu, A., Romanowsky, A. J., et al. 2018, MNRAS, 479, 3308
Amorisco, N. C., & Loeb, A. 2016, MNRAS, 459, L51
Arraki, K. S., Klypin, A., More, S., & Trujillo-Gomez, S. 2014, MNRAS, 438, 1466
Astropy Collaboration, Robitaille, T. P., Tollerud, E. J., et al. 2013, A&A, 558, A33
Beasley, M. A., Romanowsky, A. J., Pota, V., et al. 2016, ApJ, 819L, 20
Beasley, M. A., & Trujillo, I. 2016, ApJ, 830, 23
Bekki, K. 2009, MNRAS, 399, 2221
Bennet, P., Sand, D. J., Zaritsky, D., et al. 2018, ApJ, 866L, 11
Binggeli, B. 1980, A&A, 82, 289
Binney, J., & Merrifield, M. 1998, Galactic Astronomy (Princeton, NJ: Princeton Univ. Press)
Brilenkov, R., Eingorn, M., & Zhuk, A. 2015, arXiv:1507.07234
Brown, L. D., Cai, T. T., & DasGupta, A. 2001, StaSc, 16, 101
Burkert, A. 2017, ApJ, 838, 93
Caldwell, N., & Bothun, G. D. 1987, AJ, 94, 1126
Carleton, T., Errani, R., Cooper, M., et al. 2019, MNRAS, 485, 382
Chilingarian, I. V., Afanasiev, A. V., Grishin, K. A., Fabricant, D., & Moran, S. 2019, ApJ, 884, 79
Conselice, C. J. 2018, RNAAS, 2, 43
Conselice, C. J., Gallagher, J. S., III, & Wyse, R. F. G. 2003, AJ, 125, 66
Cortese, L., Gavazzi, G., Boselli, A., et al. 2006, A&A, 453, 847
Danieli, S., van Dokkum, P., Conroy, C., Abraham, R., & Romanowsky, A. J. 2019, ApJ, 874L, 12
De Lucia, G., Weinmann, S., Poggianti, B. M., Aragón-Salamanca, A., & Zaritsky, D. 2012, MNRAS, 423, 1277
Di Cintio, A., Brook, C. B., Dutton, A. A., et al. 2017, MNRAS, 466L, 1
Eigenthaler, P., Puzia, T. H., Taylor, M. A., et al. 2018, ApJ, 855, 142
El-Badry, K., Wetzel, A., Geha, M., et al. 2016, ApJ, 820, 131
Errani, R., Penarrubia, J., & Tormen, G. 2015, MNRAS, 449, L46
Ferré-Mateu, A., Alabi, A., Forbes, D. A., et al. 2018, MNRAS, 479, 4891
Foreman-Mackey, D., Hogg, D. W., Lang, D., & Goodman, J. 2013, PASP, 125, 306
Franx, M., Illingworth, G., & de Zeeuw, T. 1991, ApJ, 383, 112
Goodman, J., & Weare, J. 2010, CAMCS, 5, 65
Governato, F., Brook, C., Mayer, L., et al. 2010, Natur, 463, 203
Graham, A. W., & Driver, S. P. 2005, PASA, 22, 118
Greco, J. P., Greene, J. E., Price-Whelan, A. M., et al. 2018, PASJ, 70, S19
Gu, M., Conroy, C., Law, D., et al. 2018, ApJ, 859, 37
Hunter, J. D. 2007, CSE, 9, 90
Impey, C., Bothun, G., & Malin, D. 1988, ApJ, 330, 634
Janssens, S., Abraham, R., Brodie, J., et al. 2017, ApJ, 839L, 17
Jiang, F., Dekel, A., Freundlich, J., et al. 2019, MNRAS, 487, 5272
Jones, E., Oliphant, T., Peterson, P., et al. 2001, SciPy: Open Source Scientific Tools for Python, v1.2.2, http://www.scipy.org/
Kawata, D., & Mulchaey, J. S. 2008, ApJ, 672, L103
Kazantzidis, S., Mayer, L., Callegari, S., Dotti, M., & Moustakas, L. A. 2017, ApJ, 836, L13
Larson, R. B., Tinsley, B. M., & Caldwell, C. N. 1980, ApJ, 237, 692
Lee, M. G., & Jang, I. S. 2016, ApJ, 831, 108
Lee, M. G., Kang, J., Lee, J. H., & Jang, I. S. 2017, ApJ, 844, 157
Leisman, L., Haynes, M. P., Janowiecki, S., et al. 2017, ApJ, 842, 133
Liao, S., Gao, L., Frenk, C. S., et al. 2019, MNRAS, 490, 5182
Lisker, T., Glatt, K., Westera, P., & Grebel, E. K. 2006, AJ, 132, 2432
Mancera Piña, P. E., Aguerri, J. A. L., Peletier, R. F., et al. 2019, MNRAS, 485, 1036
Mancera Piña, P. E., Peletier, R. F., Aguerri, J. A. L., et al. 2018, MNRAS, 481, 4381
Martin, G., Kaviraj, S., Laigle, C., et al. 2019, MNRAS, 485, 796
Martín-Navarro, I., Romanowsky, A. J., Brodie, J. P., et al. 2019, MNRAS, 484, 3425
Mayer, L., Governato, F., Colpi, M., et al. 2001, ApJL, 547, L123
Mayer, L., Kazantzidis, S., Mastropietro, C., & Wadsley, J. 2007, Natur, 445, 738
McConnachie, A. W. 2012, AJ, 144, 4
McGee, S. L., Balogh, M. L., Bower, R. G., Font, A. S., & McCarthy, I. G. 2009, MNRAS, 400, 937
Mihos, J. C., Durrell, P. R., Ferrarese, L., et al. 2015, ApJL, 809, 21
Miller, R. G. 1966, Simultaneous Statistical Inference (Berlin: Springer)
Moore, B., Katz, N., Lake, G., et al. 1996, Natur, 379, 613
Müller, O., Rich, R. M., Román, J., et al. 2019, A&A, 624L, 6
Muratov, A. L., Kereš, D., Faucher-Giguère, C.-A., et al. 2015, MNRAS, 454, 2691
Ogiya, O. 2018, MNRAS, 480L, 106
Padilla, N. D., & Strauss, M. A. 2008, MNRAS, 388, 1321
Peng, C. Y., Ho, L. C., Impey, C. D., & Rix, H.-W. 2002, AJ, 124, 266
Peng, C. Y., Ho, L. C., Impey, C. D., & Rix, H.-W. 2010, AJ, 139, 2097
Peng, E., & Lim, S. 2016, ApJ, 822L, 31
Peng, Y.-J., Lilly, S. J., Renzini, A., & Carollo, M. 2012, ApJ, 757, 4
Pontzen, A., & Governato, F. 2012, MNRAS, 421, 3464
Prole, D. J., Hilker, M., van der Burg, R. F. J., et al. 2019, MNRAS, 484, 4865
Read, J. I., & Gilmore, G. 2005, MNRAS, 356, 107
Rodríguez, S., & Padilla, N. D. 2013, MNRAS, 434, 2153
Rodriguez-Gomez, V., Genel, S., Vogelsberger, M., et al. 2015, MNRAS, 449, 49
Rodriguez-Gomez, V., Sales, L. V., Genel, S., et al. 2017, MNRAS, 467, 3083

Román, J., & Trujillo, I. 2017a, MNRAS, 468, 4039
Román, J., & Trujillo, I. 2017b, MNRAS, 468, 703
Rong, Y., Guo, Q., Gao, L., et al. 2017a, MNRAS, 470, 4231
Rong, Y., Jing, Y., Gao, L., et al. 2017b, MNRAS, 471L, 36
Rong, Y., Li, H., Wang, J., et al. 2018a, MNRAS, 477, 230
Rong, Y., Liu, Y., & Zhang, S.-N. 2016, MNRAS, 455, 2267
Rong, Y., Mancera Piña, P. E., Tempel, E., Puzia, T. H., & De Rijcke, S. 2020a, MNRAS, 498, L72
Rong, Y., Puzia, T. H., Eigenthaler, P., et al. 2019, ApJ, 883, 56
Rong, Y., Yang, H., Zhang, H.-X., et al. 2018b, arXiv:1806.10149
Rong, Y., Yi, S.-X., Zhang, S.-N., & Tu, H. 2015a, MNRAS, 451, 2536
Rong, Y., Zhang, S.-N., & Liao, J.-Y. 2015b, MNRAS, 453, 1577
Rong, Y., Zhu, K., & Johnston, E. J. 2020b, arXiv:2007.12712
Roychowdhury, S., Chengalur, J. N., Karachentsev, I. D., & Kaisina, E. I. 2013, MNRAS, 436L, 104
Sánchez-Janssen, R., Ferrarese, L., MacArthur, L. A., et al. 2016, ApJ, 820, 69
Sánchez-Janssen, R., Méndez-Abreu, J., & Aguerri, J. A. L. 2010, MNRAS, 406, L65
Sánchez-Janssen, R., Puzia, T., Ferrarese, L., et al. 2019, MNRAS, 486, L1
Sandage, A., & Binggeli, B. 1984, AJ, 89, 919
Sifón, C., van der Burg, R. F. J., Hoekstra, H., Muzzin, A., & Herbonnet, R. 2018, MNRAS, 473, 3747
Spekkens, K., & Karunakaran, A. 2018, MNRAS, 475L, 116
Starkenburg, T. K., Helmi, A., & Sales, L. V. 2016a, A&A, 587, 24
Starkenburg, T. K., Helmi, A., & Sales, L. V. 2016b, A&A, 595, 56
Stewart, K. R., Bullock, J. S., Wechsler, R. H., Maller, A. H., & Zentner, A. R. 2008, ApJ, 683, 597
Struble, M. F. 2018, MNRAS, 473, 4686
Taylor, M. A., Eigenthaler, P., Puzia, T. H., et al. 2018, ApJL, 867, L15
Taylor, M. A., Puzia, T. H., Muñoz, R. P., et al. 2017, MNRAS, 469, 3444
Teyssier, R., Pontzen, A., Dubois, Y., & Read, J. I. 2013, MNRAS, 429, 3068
Toloba, E., Sand, D. J., Spekkens, K., et al. 2016, ApJL, 816, L5
Trujillo, I., Román, J., Filho, M., & Sánchez Almeida, J. 2017, ApJ, 836, 191
van den Bosch, R. C. E., & van de Ven, G. 2009, MNRAS, 398, 1117
van der Burg, R. F. J., Hoekstra, H., Muzzin, A., et al. 2017, A&A, 607, 79
van der Burg, R. F. J., Muzzin, A., & Hoekstra, H. 2016, A&A, 590, 20
van Dokkum, P. G., Abraham, R., Brodie, J., et al. 2016, ApJL, 828, L6
van Dokkum, P. G., Abraham, R., Merritt, A., et al. 2015, ApJ, 798L, 45
van Dokkum, P. G., Danieli, S., Abraham, R., Conroy, C., & Romanowsky, A. J. 2019, ApJ, 874L, 5
van Dokkum, P. G., Danieli, S., Cohen, Y., et al. 2018, Natur, 555, 629
Venhola, A., Peletier, R., Laurikainen, E., et al. 2017, A&A, 608, 142
Venhola, A., Peletier, R., Laurikainen, E., et al. 2018, A&A, 620, 165
Vijayaraghavan, R., Gallagher, J. S., & Ricker, P. M. 2015, MNRAS, 447, 3623
Vijayaraghavan, R., & Ricker, P. M. 2013, MNRAS, 435, 2713
Wheeler, C., Phillips, J. I., Cooper, M. C., Boylan-Kolchin, M., & Bullock, J. S. 2014, MNRAS, 442, 1396
Wilson, E. B. 1927, J. Am. Stat. Assoc., 22, 209
Wittmann, C., Lisker, T., Ambachew Tilahun, L., et al. 2017, MNRAS, 470, 1512
Yagi, M., Koda, J., Komiyama, Y., & Yamanoi, H. 2016, ApJS, 225, 11
Yozin, C., & Bekki, K. 2015, MNRAS, 452, 937
Zabludoff, A. I., & Mulchaey, J. S. 1998, ApJ, 496, 39